Extreme-ultraviolet High-Harmonic Generation from Structured Silica

By

Zhuang-Yan Zhang

in partial fulfilment of the requirements for the degree of

Master of Science
in Materials Science and Engineering

at the Delft University of Technology,
to be defended publicly on Thursday July 16, 2020 at 13:00 PM.

Supervisor:	Dr. P. M. Kraus	ARCNL
	Assoc. Prof. M.H.F Sluiter	TU Delft
Thesis committee:	Prof. W.M.J.M. Coene	TU Delft
	Assist. Prof. P. Dey	TU Delft

TU Delft

ARCNL

Abstract

This thesis demonstrates the feasibility of Extreme-ultraviolet (XUV) high-harmonic generation from structured silica, and was performed at the Advanced Research Centre for Nanolithography (ARCNL). The project focuses on High-harmonic generation (HHG) from condensed matter, and further explores the possibility of high-harmonic generation from micro- and nano-structured silica. HHG from solids was discovered less than a decade ago, and it is expected to be a new source for coherent ultrafast pulses, showing potential in many applications such as HHG spectroscopy, imaging and photonic devices. By generating high-harmonics in structured solids, the capability to control HHG properties by engineering the topology of the surface on solids has been demonstrated. Previous research has demonstrated the control of HHG in the visible light regime by generating from structured semiconductors. In this project, we aim to generate high-harmonics in the XUV regime, and control the properties of XUV light. Our work shows the potential of using structured dielectric materials as new XUV optics, and applications on HHG high-resolution lens-less imaging.

In chapter 1, the fundamental concepts of solid state HHG are discussed and the literature relevant for this project is summarized. Comparisons between gas-phase HHG and solid state HHG are made, and the state of the art of the previous studies, particularly on structured solid HHG, is described.

In chapter 2, the motivation and aim of this project are given.

In chapter 3, the basic theoretical method regarding to the computational method is shown, and the details about the experimental setup and sample preparation are explained.

In chapter 4, we demonstrate the experimental results which were accomplished with infrared femtosecond pulses on structured silica. High harmonics up to the 13^{th} order with photon energies of 20 eV (62-nm) were generated. We successfully controlled the spatial properties of high-harmonics in the XUV, and acquired diffraction from XUV HHG from complex patterns. Our work proved to be a promising approach to modulate XUV light at will, and added a great perspective of high-resolution lens-less imaging by using HHG from solids.

Contents

1

Introduction

High-Harmonic Generation (HHG) is a non-linear optical process in strong laser fields. It is the up-conversion of many infrared photons into one extreme-ultraviolet (XUV/EUV) photon through the non-linear interaction between an atom and an intense laser field [1]. Broadband extreme-ultraviolet light is abbreviated XUV, whereas EUV refers to narrowband light at 92 eV (13.5 nm) specifically. Due to the nature of the high-harmonic generation (HHG) process, it leads to coherent light sources and gives the rise to the field of attophysics [2]. It is the most common approach to generate XUV photons and attosecond pulses. The combination of HHG in the XUV regime equips the technique with extremely high temporal and spatial resolution. One of the great examples is the use of HHG for optical metrology in EUV lithography. Here, HHG is used to generate EUV photons for the inspection of EUV masks [3, 4]. By using femtosecond infrared pulses, ultrafast XUV attosecond pulses can be generated, for attosecond spectroscopy [5, 6] as well. Attosecond spectroscopy is widely applied to investigate electron dynamics in condensed matter and the underlying mechanisms of chemical reactions [7]. Moreover, the coherent nature of pulses from HHG is a key for applying high harmonics in optical imaging. The discovery of HHG was not only a milestone for non-linear optics, but also contributes to the development of other academic fields. The field of HHG has significant industrial applications and provides a boost to economy.

Harmonic generation was first observed with CO2 laser in 1977 [8]. Harmonics up to 11^{th} order (1.29 eV) were generated but it was below the ionization potential of the generation medium Aluminum (5.98 eV). High-order harmonic generation is a strong field process and it only occurs when the strength of the applied electric field is comparable to the strength of binding energy of electrons in the atomic potential. Due to its low conversion efficiency and high requirements on experimental setups, it was not discovered until 1987, when McPherson et al. aimed to detect the fluorescence emitted from noble gases but accidentally obtained HHG up to 17^{th} order in Neon [9]. At the time, this phenomenon could only be partially explained using the knowledge of non-linear optics in a perturbative framework, and the characteristics of the observed spectra could not be explained by perturbative non-linear optics [10, 11]. A full theory of high-harmonic generation only came a few years later, which explained a perturbative region where the intensity of HHG follows the classic low-order

harmonic generation, a plateau where the conversion efficiency (CE) remains constant with increasing non-linear orders, and a cutoff region where the CE drop rapidly within a couple of non-linear orders [1, 12]. Meanwhile, the three-step model was theorized and validated, which provided an insightful intuition to the HHG process. , The work of Lewenstein's [13] helped in combining the quantum tunneling theory with a classical electrodynamic description.

Nowadays, high-harmonic generation (HHG) from noble gases or plasmas is well understood and gas-phase HHG remains the main XUV source for both fundamental studies and industrial applications. Recently, experiments demonstrated a novel way to generate high harmonics in condensed matter [14, 15, 16]. In 2011, the first HHG from solids was observed by Ghimire et al. [14]. It was the first time that high-harmonics were observed in bulk materials. The HHG in solids occurs below the damage threshold of the materials. The experiments were performed in ZnO with mid-infrared pulses, and obtained HHG spectrum covered the range from 3 to 9 eV. Subsequently, HHG from condensed matter was first carried out in XUV regime by Luu et al. [15] in 2015. Coherent ultraviolet radiation was accomplished in a sculpted sub-cycle field and was emitted with a photon energy up to 31 eV from a thin SiO_2 film. Very recently in 2018 [16], high-harmonics up to 34 eV were first generated from solids with a more conventional and commercially available femtosecond infrared laser. Several theoretical models, based on the time-dependent Schrödinger equation and semiconductor Bloch equations [17, 18, 19, 20], were established to understand the mechanism driving the HHG process in solids. It has been found that interband polarization and intraband current are two primary contributing factors to HHG in solids. Solid-state HHG not only provides a XUV source, but also links strong-field optical physics to solid-state physics. The developments in the field of solid state HHG allows one to come up with flexible and creative ideas, e.g. HHG from structured solids yielding new insights for photonics. A direct emission from engineered solids offers an intriguing method to control the temporal or spatial properties of XUV. Together with ultraviolet radiation, XUV high-harmonic generation from structured solids shows great potential for ultrafast photonics and XUV optics. [21, 22, 23]

1.1 Principle of High-Harmonic Generation

1.1.1 Extreme nonlinear optics

The beginning of the field of non-linear optics follows the invention of the laser in 1960 by Maiman [24]. The first non-linear optical response that was discovered is second harmonic generation by Franken et al. in 1961 [25]. The phenomena "nonlinear" is the response of materials to an applied optical field depending in a nonlinear manner on the strength of the optical field. Optical nonlinearity can be quantified by the dipole

moment in a unit volume, or so to speak polarization $P(t)$. Under application of a low electrical field, there is a linear relationship between polarization and electrical field,

$$P = \varepsilon_0 \chi E, \tag{1.1}$$

where ε_0 is the permittivity and χ is the linear susceptibility.

However, under strong fields, the nonlinear terms in the induced polarization become more important. The polarization can be expressed by the Taylor series:

$$P = \varepsilon_0 \chi^{(1)} E + \varepsilon_0 \chi^{(2)} E^2 + \varepsilon_0 \chi^{(3)} E^3 + \cdots, \tag{1.2}$$

where the quantities $\chi^{(2)}$ and $\chi^{(3)}$ are second- and third-order electric susceptibilities. The first term defines the linear susceptibility, the second term defines the lowest order nonlinear susceptibility, and so on.

High-harmonic generation is an extremely nonlinear optical process which occurs only in a strong field regime. This requires a peak intensity of the fundamental beam with at least 10^{12} W/cm^2 for solids and 10^{13}~10^{15} W/cm^2 for gases, which can be achieved by focusing high power femtosecond pulses. During the HHG process, the contribution of the very high order nonlinearities becomes significant. With even higher peak intensity (10^{13} W/cm^2), the electric field becomes comparable to the atomic coulomb field, and the perturbation theory is no longer valid. Such extreme nonlinearity allows subdivision of the laser period. Once the intensity enters the non-perturbative regime, the efficiency of high-harmonic generation as a function of the emitted photon energy remains nearly constant over a broad range of photon energies, and a nonlinear polarization description holds no more.

1.1.2 Gas-phase HHG

Three step model

Since the discovery of high-harmonic generation, many efforts have been made to describe the mechanism of HHG. The three-step model is recognized to give a clear explanation of the interaction between atoms and a strong electric field and to predict features of gas-phase HHG. In the first step, the Coulomb potential of an electron bound to an atom is bent using a strong electric field so that electrons can be ionized and tunnel through the potential barrier. After an electron has tunneled out, it can be considered as a free particle in the electric field. Free electrons are accelerated under the electric field and generate a wave pack in the continuum. When the electric field changes its sign, some electrons are pulled back towards the parent ions and upon recollision of the electron with the parent ion, extreme ultraviolet photons can be

emitted with the energy that equals the ionization energy plus the electron kinetic energy at return.

Ionization in a strong field

The gas-phase harmonic yield is directly related to the ionization rate, or the population of free carriers. Ionization is classified into multiphoton or tunneling ionization, which are two limiting cases. Multiphoton absorption preferentially occurs under short wavelengths and low intensities while tunneling ionization occurs under long wavelengths and high intensities. In reality, most cases have the characteristic of both. The Keldysh parameter describes the transition between these two regimes. It is written as:

$$\gamma = \sqrt{\frac{I_p}{2U_p}}, \tag{1.3}$$

where I_p is the ionization potential, U_p is the ponderomotive potential.

For $\gamma \gg 1$, multiphoton absorption is more relevant and the ionization rate scales as:

$$r_{multiphoton} \propto I^n, \tag{1.4}$$

where n is the number of photons and I is the intensity of the laser field.

For $\gamma \ll 1$, tunneling ionization applies and the ionization rate scales as:

$$r_{tunneling} \propto e^{-\frac{2}{3}\frac{I_p^{3/2}}{E}}, \tag{1.5}$$

where E is the field strength in atomic units.

Propagation and recollision

After ionization, the electrons propagate in an electric field. The obtained kinetic energy of the electrons is based on the time of ionization and recollision. According to their traveling time in the continuum, the electrons' trajectories are identified as short and long trajectories. Long trajectories ionize earlier and recombine later within the driving laser field compared to short trajectories, but lead to the same energy as short trajectories do. Towards the time when the electrons emit the highest photon energy, short and long trajectories converge and are not distinguishable at that point anymore. Different propagating time of electrons in continuum also leads to different optical properties between short and long trajectories in terms of divergence and coherence [26]. Therefore, gas-phase harmonic generation exhibits an intrinsic chirp at the sub-

cycle level, which means harmonic orders carrying different photon energies are emitted at different time within an optical cycle [27].

The maximum emitted photon energy in a gas is

$$E_{max} = I_p + 3.17U_p, \tag{1.6}$$

where U_p denotes the pondermotive energy, equal to [28]

$$U_p = \frac{\alpha_{FS}\hbar I\lambda^2}{2\pi c^2 m}, \tag{1.7}$$

where α_{FS} is the fine structure constant, m is the electron mass, c is the speed of light and λ is the laser wavelength.

Quantum mechanics models

The time-dependent Schrödinger equation provides the most accurate quantum mechanical description of the atom behavior in a strong field. In the strong-field approximation (SFA), the coulomb potential can be neglected since the electric field dominates the motion of electrons over the propagation. The most popular quantum description is the Lewenstein model, which provides deeper insights into the process of HHG. The Lewenstein model concentrates on the XUV radiation which is emitted during the recollision. It has the following assumptions: 1) in a strong field, the excited bound states have no contribution to the wave packet and their population can be neglected, 2) the electrons' evolution is not affected by the coulomb potential. [13]

The time-dependent wave function can be written as a superposition of the ground-state wave function and the continuum wave function [2]:

$$\psi = \psi_b + \psi_c = a(t)e^{iI_p t}|\psi_g\rangle + \int d^3\vec{v}\, b(\vec{v},t)|\,\vec{v}\rangle, \tag{1.8}$$

where $|\psi_g\rangle$ represents the ground-state wave function and $|\overrightarrow{v}\rangle$ represents the atomic state with one continuum electron of velocity of $\vec{v}$. The time varying dipole moment of total emission can be expressed as [2]:

$$\vec{d}(t) = \langle\psi_b|\vec{r}|\psi_b\rangle + \langle\psi_c|\vec{r}|\psi_c\rangle + \langle\psi_b|\vec{r}|\psi_c\rangle + \langle\psi_c|\vec{r}|\psi_b\rangle. \tag{1.9}$$

The first term represents the permanent dipole moment in the ground state that vanishes for an atom. The second term represents the dipole moment during the electrons' acceleration in the continuum, which is negligible compared to the third and fourth terms which represent the recombination of electrons in the continuum to and

from ground state respectively. The acceleration of the dipole moment can be Fourier transformed to the HHG spectrum.

Every half cycle gives a harmonic burst and within one cycle consecutive bursts are generated with the same amplitude but out of phase. Therefore, even order harmonics destructively interfere with each other, and odd order harmonics constructively interfere. That is the reason that, in the end, the emitted frequencies are odd integer multiples of the frequency of the driving field.

Conversion efficiency in gas-phase HHG

High harmonic generation from gases has a fairly low conversion efficiency of about 10^{-6}. The low CE is attributed to low recombination of electrons since most of free electrons are ionized at the peak of the pulses. Moreover, gas atoms have very large free space thus leading to a low density. To obtain higher order nonlinearities, higher laser intensity with high repetition rate is required. However, there is an upper limit of laser intensity for plasma HHG. If the laser intensity is too high, optical breakdown will suppress the HHG process when ionization reaches a critical value and gets saturated, and gaseous media becomes opaque to the pumping laser radiation. Therefore, timely refreshing gas atoms is essential to increase conversion efficiency. However, it is limited by the manufacturing of gas jets and associated vacuum system. Operating gas-phase HHG with a very powerful laser is challenging, just as a high-intensity laser with MHz repetition rate.

Phase matching in gas-phase HHG

The observed HHG spectrum is attributed to the coherent addition of the emitted radiation through propagation. For each harmonic order q, the maximum length for constructive interference between the radiation from different atoms is defined as coherent length, $L_{coh,q} = \pi/\Delta k_q$. It depends on the mismatch vector $\Delta k_q = q k_f - k_q$, where k_f is the wavevector of the fundamental beam and k_q is the wavevector of q^{th} harmonic order. For coherent buildup of the harmonic emission, the mismatch vector has to be minimized, thus the wave fronts of the fundamental laser and the generated harmonics must be in phase. The phase mismatch is attributed to three factors. These are Gouy phase, dispersion and dipole phase. Gouy phase is geometrical phase which originated from the gaussian beam phase along the propagation direction. Dispersion is caused when light propagates through neutral media or free-electron plasma. Dipole phase is linked to the excursion time of free-electrons propagating in the continuum. Therefore, the dipole phase is larger for the long trajectories. Since the observed HHG is the ensemble of the radiation from the different atoms in the macroscopic point of

view, phase matching in gas-phase HHG has a substantial impact and has to be taken into account in terms of HHG yield. [29]

1.2 High-harmonic generation in Solids

1.2.1 Mechanism of solid state HHG

High-harmonics in solids were discovered within the last decade, and the phenomenon occurs without the presence of plasma or ionization. Therefore, it must have a different mechanism from gas-phase HHG, which begins with ionization. Solid state HHG is attributed to two mechanisms – an interband polarisation and an intraband current – as shown in Figure 1.1.

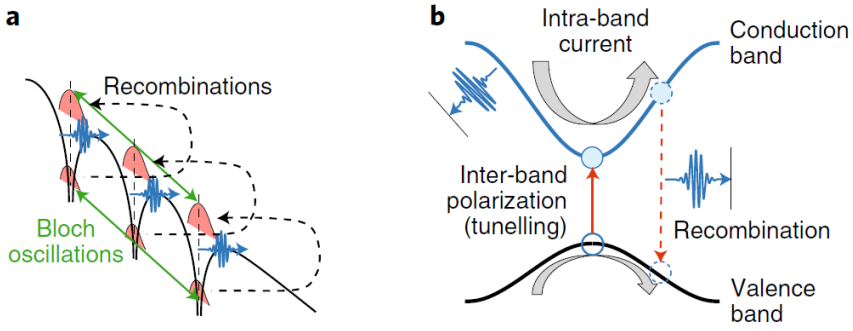

Figure 1.1 Mechanism for solid state HHG. (a) and (b) indicate the intraband radiation through Bloch oscillations and the interband polarization through the recombination of electron-hole pairs in real space and momentum space respectively. [30]

The electrons in the valence band can be excited to the conduction band by Zener tunneling or the absorption of multiple photons. Different from atomic harmonic generation, electrons will never be far away from the cores, which disagrees with the usual strong field approximation [31]. Moreover, due to the nature of the non-parabolic band structure, group velocity and effective mass of those electrons are momentum dependent. Free electrons in the continuum and holes left in the ground state interact with the incident laser field, leading to the two possible mechanisms mentioned.

Even though the mechanism varies for atomic and solid state HHG, similarities were shown and provide intriguing insights into HHG in solids, such as the propagation and recollision of electrons in the continuum [32], and the existence of short and long trajectories in solid-state HHG under the interband mechanism [33] [34]. Under these observations, it is claimed that high-harmonics from interband polarization exhibit atto-chirped features which is related to laser parameters and band structures, while those from intraband emission are chirp-free [35] [36] [37].

Perturbative and non-perturbative nonlinearity

The spectrum for gas-phase HHG features a burst of pulses of low-order harmonics followed by a plateau of high-order harmonics. As mentioned above, this indicates two different nonlinear regimes defined by the Keldysh parameter. In solid-state HHG, there are no ionized electrons. It has been experimentally shown that HHG in solids follows a perturbative regime in weak electric fields and a non-perturbative regime in very intense electrical fields [14, 15, 22] [38, 39, 40, 41]. The Keldysh parameter can be adjusted by altering the ionization potential to the bandgap energy, expressed as [42]

$$\gamma = \omega \frac{\sqrt{2m\mathrm{E_g}}}{eF}, \tag{1.10}$$

where ω, F and E_g are the laser frequency, maximum field strength and bandgap respectively, e is electron charge and m is the reduced mass of an electron and a hole ($m^{-1} = m_e^{-1} + m_h^{-1}$). This description can be used to estimate whether the HHG process in condensed matter is under a perturbative or a non-perturbative regime.

Cut-off energy

In atomic HHG, the cut-off energy is related to the wavelength and the peak field of laser pulses. In solid state HHG, the cut-off energy shows linear scaling with the peak field [14], and strongly depends on the band structure of the materials [30]. It has been shown that materials with higher bandgap might give higher cut-off signals [30]. According to the interband model, the cut-off energy should be limited to the maximum band gap at the Brillouin zone. As driven electrons gain more energy, they may escape the first Brillouin zone and be promoted to higher-lying conduction bands [43], leading to a new plateau and associated cut-off energy. According to the intraband emission, the cut-off energies are not constrained by the first conduction band, and electrons are able to tunnel to higher conduction bands, which may also give different plateaus and cut-off energies. The cut-off energies in the intraband model are attributed to the shape of the conduction bands and the driving peak field, as the Bloch frequency equals to $\omega_b = \frac{eF_0 a}{\hbar}$, where F_0 is the field intensity.

Conversion efficiency in solid state HHG

Condensed matters have densely packed electrons, thus, solid-state HHG is expected to have higher conversion efficiency (CE) despite low driving intensity and absence of ionization. The upper limit of the laser intensity for solid state HHG is defined by the damage threshold of the solid samples. Damage can be due to thermal expansion or dielectric breakdown, and is highly dependent on geometries, chemical compositions, crystal structures and qualities of the specimens. Dielectric breakdown is the most dominated damage mechanism and it occurs before the intensity of electrical field is sufficient for ionization. Therefore, the formation of a long-lived

plasma which limits the gas-phase HHG CE at high repetition rates is no longer a concern in solid state HHG. Therefore, in principle, more powerful laser systems might be allowed for solid state HHG.

Phase matching in solid state HHG

In solid-state HHG in the extreme ultraviolet, phase matching is relaxed compared to gas-phase HHG, owing to the short penetration length of high-harmonic radiation in materials. Therefore, only high harmonics emitted from the surface contribute to the observed HHG spectrum [44]. The attenuation lengths of different photons are less than their wavelengths. For example, with a fundamental beam of 800 nm, the 7^{th} order harmonic has a wavelength of 114 nm and an attenuation length of 17 nm in fused silica, while the 6^{th} order harmonic has a wavelength of 133 nm and an attenuation length of 96 nm.

Breaking of inversion symmetry in HHG

Natural HHG processes in gas atoms lead to only constructive interference of odd harmonics. Even order harmonics can only be generated when there is an inversion symmetry of the dipole moment under the Hermitian operator. In gas-phase HHG, even-harmonic emission can be achieved by using two laser pulses to break the inversion symmetry of the electric field within an optical cycle. In condensed matter, inversion symmetry intrinsically exists in crystals. Many researchers reported the generation of even-order harmonic along different crystal orientations, where an antisymmetric optical field is built in the spatial domain. [41, 45, 46]

Motivation of solid state HHG

By comparing gas-phase HHG to solid-state HHG, solid state HHG requires a vacuum system with relaxed requirements. It might be further optimized to once exceed the conversion efficiency of gas-phase HHG, and allowed to be operated with extremely powerful laser systems. The inversion symmetry can easily be broken by choosing suitable materials. Moreover, HHG in solids provides a new approach to investigating novel optical applications. Particularly, it shows potential to directly control HHG properties by engineering the topology of solids.

1.2.2 Outlook on Solid HHG

Pervious research on mechanisms of solid HHG

The mechanism driving the HHG process in solids is not yet fully understood. The contribution from interband and intraband are under debate. Combining quantum mechanics with the semiclassical model, many publications showed that the

dominance of one mechanism over the other may be highly material-dependent [15] [32] [36] [37] [39] [43] [47] [48].

The work of G. Vampa et al. [32] shows that high-harmonic generation is mainly attributed to interband radiation. When they focus mid-infrared laser pulses with a central wavelength of 3.76 μm, and the second harmonic of it on a 500 nm ZnO thin sample, they observe the different perturbation between even and odd harmonic spectrum. Different harmonic orders are enhanced at different time-delays between two pulses. Comparing experimental results with simulations leads to the statement that interband polarisation is the primary source of high-harmonic generation in ZnO in their experiments.

T. Luu et al. [15] indicates that high-harmonic generation in SiO_2 is reasonably reproduced by intraband current only. They solved a classical model including interband acceleration of carriers and obtained results that agree with the intraband model and disagree with the interband. Simulations also showed that higher conduction bands did not play a critical role in this picture. By increasing the number of involved conduction bands in their simulations, the results did not vary much. Moreover, the semi-classical model yields better simulations than the quantum-mechanical model. This gives additional evidence that the intraband current is coupled with interband polarisation in the semiconductor Bloch equations.

In a two-band model, emission of interband harmonics occurs when the harmonic photon energy matches the instantaneous field-dressed bandgap [37, 49], $\varepsilon(t) = 2\hbar\sqrt{(\mu E(t))^2 + \left(E_g/2\right)^2}$, where μ is the transition dipole matrix element, $E(t)$ is the time-dependent field, and E_g is the bandgap. In the few cycle limit, the large variation of electric field in amplitude in consecutive half-cycles leads to a different value of $\varepsilon(t)$. If a value of $\varepsilon(t)$ is reached at a certain time t in a half-cycle, in the subsequent half-cycle, the same value can be reached again at a time $t + T/2$, where T is the laser period. Y. You et al. [37] used the same high-harmonic spectroscopy and observed a CEP-related photon-energy shift in MgO. With higher photon energy, this energy shift by changing CEP became more obvious. That clearly shows the chirp feature of high-harmonics in MgO. It proved that the mechanism driving high harmonic generation in MgO agrees with the interband model. Further, the second plateau was observed as well, which is additional evidence for the interband mechanism. Apart from Y. You's work, O. Schubert's [47] and M. Garg's work [48] observed no energy shift with CEP change in GaSe and SiO2.

In subsequent work [39], S. Han et al. demonstrate experiments which are done in a multi-photon regime, by applying a laser source of 12 fs with a central wavelength of

800 nm, at 75 MHz repetition rate to 430 μm Sapphire (Al_2O_3) substrates. The band structure of the sapphire sample has been simulated along different crystal orientations, and the HHG spectra were observed along all crystal orientations. Since the k-vector along a certain crystal orientation is significantly shorter, intraband currents would contribute to a much higher frequency, while experimental results only showed a cut-off energy close to that shown in interband model.

In the work of A. J. Uzan et al. [43], they showed other models that involved multiband emission. They indicated that high-lying conduction bands coupled with a valence band lead to high-harmonic generation under the interband mechanism. They claim that at Van Hove singularity, where electrons and holes are most likely recombined, are the main factor contributing to the HHG spectrum. Emitted photon energies are associated with energy gaps between the critical points of conduction bands and valence bands. Experiments showed the match of photon energies to the simulated band structures. Along different crystal orientations, the momentum vector changes and the HHG spectrum shows the enhancement of certain photon energies while others disappeared.

The debate about the mechanisms for high-harmonic generation in the solid state is still on-going. From past research, it can be seen that there is good evidence for both mechanisms, while the dominating factor may be highly material dependent.

Literature review on structured solid state HHG

Since the discovery of solid-state HHG, there has been an increasing amount of studies related to the field. One of the exciting perspectives of solid-state HHG is to control HHG properties by engineering the topologies of materials. Structures can be designed by altering the chemical compositions or morphology of materials to change the local field or wave front, thus modifying the HHG properties at will. There is some relevant research which gives illustrations on this topic and yields insights about this work.

In 2013, M. Sivis et al. [50] showed gas-exposed plasmonic bow-tie nanoantenna for the EUV HHG generation, where the nano bow-tie structures were expected to locally enhance the driving field and therefore enable coherent build-up of EUV radiation, thus raising the intensity of coherent HHG and distinguishing it from atomic line emission fluorescence. Even though there are constrains to coherent build-up, it demonstrates the feasibility of strong-field phenomena in an optical near-field. It opens up the study of radiation and optical coupling effects within nanostructures at XUV and EUV frequencies.

A subsequent study by S. Han et al. in 2016 [51] observed field enhancement and generated HHG up to 60 nm from metal-sapphire nano-cone structures. The sapphire

cone was coated with gold on the side, which only allowed emission from an uncoated tip of sapphire. Enhancement from metallic-semiconductor hybrid structures, like an array of Au nano-rods [40] [52], were demonstrated by other studies as well. The plasmonic resonances ensure the local field enhancement with sub-diffraction-limited spots on the sapphire tip therefore increasing conversion efficiency of the HHG process. Similarly, nano-cone structures based on all-semiconductor materials were fabricated by D. Franz et al. [21], where a nanoscale size HHG source was created by illuminating a single nano-cone (2 µm, 19 MHz, 8.7 nJ, 85 fs). Such HHG sources are promising to use as nano-probe in nano-tomography. In their study, they further showed possibility of using HHG from nano-cone as a pointy light resource for imaging. The enhancement of HHG in a regime beyond the bandgap of the material (ZnO) was investigated.

H. Liu et al. [22] made metasurfaces from all-dielectric materials. Where they have bar and disk of a size comparable with half the wavelength of the incident laser pulses (2.3 µm, 1 kHz, 70 fs), the HHG generated from the substrates shows a great enhancement of harmonic emission due to a fano-resonance. The numerically determined resonance wavelength for bars and disks are 2318 nm and 2321 nm (bar mode and disk mode). By illuminating the sample with chirped pulses, radiation from bars and disks shifted over time, leading to a temporal dispersion from these two modes. For higher-order harmonic the enhancement is more significant than lower-order harmonics under a non-perturbative regime. These results exhibit the control of the HHG process in the temporal and frequency domains, which enables high harmonics with narrower linewidth, longer coherence and longer temporal duration, as well as the control of amplitude and phase from anisotropic nano-structures.

Polarization dependent emission is among the interesting properties of high-harmonics generated on structured solids. Among all these asymmetric nano structures, such as nanoantennas and said disks/bars structures, the enhancement of HHG are extremely polarization dependent. G. Vampa et al. [40] demonstrated the polarization dependent enhancement of HHG from Au nanoantenna structures on silicon crystal. The coupling plasmonic effect is only present when the polarization is along the major axis of the nanoantennas, leading to a 10 times higher signal on the 5^{th} and 7^{th} harmonic and a new peak on the 9^{th} harmonic (233nm), which was below the noise level when it was generated from a bulk sample. In their later study [53], where Au electrodes in line shape were fabricated on a ZnO or Si substrate, they controlled the polarization dependent local emission around electrodes by applying bias voltage on the electrodes. By breaking inversion symmetry of the electric field the 4^{th} order harmonic was observed, and their study demonstrates the basic control over the beam profile of 4^{th} harmonics. It shows the possibility to achieve a tailored field distribution by reasonably designing structures. By controlling and dominating the emission from

even harmonics, it potentially enables us to reach a high spatial resolution. Meanwhile chemically specific imaging can also be achieved.

M. Sivis et al. [23] have demonstrated spatial control of HHG by changing the morphology and chemical composition of materials. HHG were generated on a Fresnel Zone plate which consists of two different chemical compositions (Si and Ge-doped Si), and ZnO cone structures. The wavelength dependent diffraction patterns were recorded from both samples. It shows a strong enhancement and self-focusing of each harmonic order on HHG spectrum due to diffraction. By using large band-gap materials and short wavelength incident laser pulses, the HHG emission can extend to the XUV wavelength range to reach high spatial resolution for imaging. Along with the results from H. Kim et al. [54] – EUV radiation from a sloped surface of sapphire is reflected with the same reflection angle of the driving IR laser based on Snell's law – the phase shift from this Fresnel zone plate and other propagation profiles of HHG from engineered materials may also help to better understand the underlying mechanisms of the HHG process.

All these experiments showed the great potential of HHG from structured solids, in terms of increasing conversion efficiency and controlling the polarization, temporal and spatial properties of HHG. They illustrate its potentially significant industrial value. The flexibility of solid-state HHG may boost a new generation of ultrafast optoelectronics, electrically gate-able tailored light sources for spectroscopy, microscopy and attosecond physics.

2

Motivation and Aim

High-Harmonic generation in condensed matter is an emerging field that has only been discovered in the last decade. The coherent nature of the HHG process is an essential characteristic for an optical light source. Solid-state HHG from structurally engineered materials raises the possibility of directly shaping the beam at the generation medium, as well as imaging complex structures by recording coherent diffractive emission patterns. Such advances will find wide-spread applications in ultrafast optics, optical electronics or lens-less imaging. HHG in XUV draw special interest particularly since shorter wavelength is the key to achieve an extremely high spatial and temporal resolution in these applications. Meanwhile, a direct control of XUV properties using patterned bulk materials ease the constrains of the lack of sufficient optics at these wavelengths and the extremely short penetration depth of these wavelengths in materials.

In the previous chapter, a brief account of the basics of the HHG process in solids was given. Through the State of Art, it can be seen that the theoretical study of HHG in solids remains incomplete. XUV radiation through interband and intraband models both show strong and clear presence but can be highly material dependent. Previous research on structured solid-state HHG declared a significant interest in imaging and controlling HHG properties in space and time by plasmonic enhancement on hybrid interfaces, electrical coupling, and suitably designed optical surfaces. For example, in the study of M. Sivis et al. [23], the diffraction consisting of visible lights from structured ZnO cones was obtained. However, these researches mainly focused on the low bandgap semiconductors with a generation regime in visible light. Since they achieved HHG above the bandgap of materials, the principle should be applicable to generating XUV with high band-gap materials such as SiO_2 or Al_2O_3. Therefore, it inspired us to investigate the possibility to generate XUV from structured solid. Most materials investigated in previous studies are semiconductors (Si/ZnO) and insulators (MgO/Al_2O_3). Since the underlying mechanism is highly material dependent, and these materials are suspected to be dominated by interband HHG emission, whether or how mechanisms influence the process when generating high-harmonics from structured materials suspecting dominated by intraband current remains unclear.

In this project, we focus on HHG in the extreme-ultraviolet range and are motivated to understanding the underlying physics, design tailored attosecond extreme-ultraviolet pulses, and show the potential of XUV HHG lens-less imaging. Starting from the simplest structure – a grating – on SiO_2, we aim to control the spatial profile

of the HHG process in the XUV range, and to understand how to interpret the fundamental beam profile to HHG profile. By using subwavelength structures of SiO_2, we investigate the possibility of using XUV HHG as a fast high-resolution imaging technique. We obtain the diffraction from thin SiO_2 substrate patterned with smiley emoji, and demonstrate the great potential of fast high-resolution lens-less HHG microscopy.

3

Methods and Experiments

3.1 Theoretical methods

3.1.1 Fourier Analysis

In classic optics, light consists of electromagnetic waves. The plane wave is the simplest example of a three-dimensional wave. When the wave propagates through space, the mathematical expression for a plane wave is

$$\psi(\vec{r}, t) = Ae^{i(\vec{k}\cdot\vec{r} \pm \omega t)}, \tag{3.1}$$

where A is the wave amplitude, $\vec{k}$ is the wave vector, also called propagation vector, ω is the angular frequency. The wave vector denotes the propagation direction and its absolute value is defined as the wavenumber k, which describes the spatial frequency of a wave. We have

$$k = |\vec{k}| = \frac{n\omega}{c} = \frac{2\pi n}{\lambda}, \tag{3.2}$$

where n is the refractive index of the medium where the wave propagates.

The mathematical description of light is derived from Maxwell's equations [55]. Assuming a wave behaves like a transverse electromagnetic plane wave (i.e. $\vec{\mathcal{E}}$, $\vec{\mathcal{H}}$ and $\vec{k}$ form a mutually orthogonal triplet), then the electric and magnetic field can be expressed as

$$\vec{\mathcal{E}} = Re\{\overrightarrow{E_0}e^{i(\vec{k}\cdot\vec{r} \pm \omega t)}\}$$

$$\vec{\mathcal{H}} = Re\{\overrightarrow{H_0}e^{i(\vec{k}\cdot\vec{r} \pm \omega t)}\}, \tag{3.3}$$

where E_0 and H_0 are locally constant and have complex components.

Any three-dimensional wave can be decomposed as a series of plane waves, each having a distinct amplitude and propagation direction. By adding up more frequency components, a stronger amplitude modulation can be achieved, thus forming shorter pulses in temporal domain. Temporal spectrum can be mathematically decomposed

into its individual frequency components. This is known as Fourier transform. The Fourier transform (alternatively Fourier Spectrum) of a function $E(x,y)$ (here use electric field) is represented here by $\mathcal{F}\{E\}$ or $\hat{E}$, and is defined by

$$\mathcal{F}\{E\} = \hat{E}(k_x, k_y) = \frac{1}{2\pi} \iint_{-\infty}^{+\infty} E(x,y) e^{-i(xk_x + yk_y)} dxdy, \tag{3.4}$$

where k_x and k_y are the components of wave vectors $\vec{k}$ along the x and y direction.

Inverse Fourier transforms are defined by

$$\mathcal{F}^{-1}\{\hat{E}\} = E(x,y) = \frac{1}{2\pi} \iint_{-\infty}^{+\infty} \hat{E}(k_x, k_y) e^{i(xk_x + yk_y)} dk_x dk_y. \tag{3.5}$$

An interference pattern is yielded when plane waves overlap in space. Interference is a very common phenomenon, that consists of the coherent phase correlation between waves in temporal and frequency domain. When two waves are in phase and coherently built up, the intensity modulation can be detected in optical measurements. The intensity of a narrow band wave is given by

$$I(x,y,t) = \langle |E(\xi,\eta,t)|^2 \rangle, \tag{3.6}$$

where *P* is a certain point of wave scalar, and the angle brackets signify an infinite time average.

Fourier analysis is a ubiquitous tool that has found application, such as diffraction, imaging, optical data processing and holography.

3.1.2 Diffraction

Diffraction may be envisioned as arising from interaction between electromagnetic waves and physical obstructions. This phenomenon has first been illustrated by the work of Francesco Grimaldi in the 1600s, which he called “diffraction”. As an initial approach, Huygens-Fresnel principle are used to describe it in classical physics. It states that every unobstructed point of a wavefront, at a given instant, serves as a source of spherical secondary wavelets. The amplitude of the optical field at any point beyond is the superposition of all these wavelets. Nowadays, the computational approach based on Fourier optics allows us to better understand the behavior of light propagating through an object. It is widely used in imaging techniques. In a coherent diffractive imaging measurement, the objective is to reconstruct an image of the object based on the acquired diffraction pattern.

The Angular Spectrum

Considering that an electric field $E(x,y,z)$ propagates along the z-axis, with known $E(x,y,z_0)$, the electric field at any position along the z-axis can be calculated by a Fourier transform of its angular spectrum $\hat{E}$, expressed as

$$E(x,y,z) = \frac{1}{4\pi^2}\iint_{-\infty}^{\infty} \hat{E}(k_x,k_y,z)\mathrm{e}^{i(k_x x+k_y y)}\,dk_x dk_y. \tag{3.7}$$

The angular spectrum at position z has a representation of the form

$$A(k_x,k_y,z) = A(k_x,k_y,0)\exp\left(\frac{i2\pi}{\lambda}\sqrt{1-\alpha^2-\beta^2}\,z\right), \tag{3.8}$$

while

$$\vec{k} = \frac{2\pi}{\lambda}(\alpha\hat{x}+\beta\hat{y}+\gamma\hat{z}), \tag{3.9}$$

and

$$\gamma = \sqrt{1-\alpha^2-\beta^2}.$$

$$\alpha = \frac{k_x}{|k|}, \qquad \beta = \frac{k_y}{|k|}, \qquad \gamma = \sqrt{1-\left(\frac{k_x}{|k|}\right)^2-\left(\frac{k_y}{|k|}\right)^2}. \tag{3.10}$$

The result demonstrates that when the direction cosines (α,β) satisfy

$$\alpha^2+\beta^2 < 1, \tag{3.11}$$

as all true direction cosines must, the effect of propagation of a wave over a distance z is simply changing the relative phases of consistent waves propagating to different directions.

However, when

$$\alpha^2+\beta^2 > 1, \tag{3.12}$$

the imaginary part in Eq.(3.8) is no longer valid and it can be rewritten into

$$A(k_x,k_y,z) = A(k_x,k_y,0)\exp\left(-\frac{i2\pi}{\lambda}\sqrt{\alpha^2+\beta^2-1}\,z\right). \tag{3.13}$$

Under such condition, the wave components are rapidly attenuated by the propagation as it decays fast with the exponential term. Such components are called evanescent waves, and those waves carry no energy from the diffractive aperture.

In the end, the general expression of angular spectrum for the electric field after propagation is written as

$$E(x,y,z) = \frac{1}{4\pi^2}\iint_{-\infty}^{\infty} \hat{E}(k_x,k_y,z)\, e^{i|k|z\sqrt{1-\left(\frac{k_x}{|k|}\right)^2-\left(\frac{k_y}{|k|}\right)^2}} \times e^{i|k|(k_x x+k_y y)} dk_x dk_y, \tag{3.14}$$

where the evanescent wave phenomenon is effectively limiting the region of integration to the region where Eq. (3.11) is satisfied. This gives the fundamental explanation that no conventional imaging system can resolve a periodical structure with a period which is finer than the wavelength of incidence.

Propagation of the angular spectrum provides a generally applicable method to obtain a diffraction of light. There are other approximations which are more convenient to approach a relatively fast computational algorithm in reality, which are the Fresnel approximation and the Fraunhofer approximation.

The Huygens-Fresnel Principle

Now we assume a diffraction aperture in the (ξ,η) plane and it is illuminated by light along the orthogonal direction of the plane. The wavefield across the (x,y) plane, which is parallel to the (ξ,η) plane and at a normal distance z from it, can be obtained based on Huygens-Fresnel principle. The Huygens-Fresnel principle can be stated as

$$E(x,y) = \frac{z}{i\lambda}\iint_{\Sigma} E(\xi,\eta)\frac{e^{ikr_0}}{r_{01}^2} d\xi d\eta, \tag{3.15}$$

where Σ is the aperture, r_{01} is the vector pointing from (x,y) to (ξ,η), and it is given by

$$r_{01} = \sqrt{z^2 + (x-\xi)^2 + (y-\eta)^2}. \tag{3.16}$$

The Huygens-Fresnel principle is derived from Green's theorem and the integral theorem of Helmholtz and Kirchhoff. Two assumption are made to reach Eq. (3.16). The first one is the approximation inherent in the scalar theory. The second one is that the observation distance is far from the aperture, $r_{01} \gg \lambda$. Fresnel and Fraunhofer approximation are subsequent expression based on Huygens-Fresnel principle.

The Fresnel approximation and Fraunhofer approximation

When the observing plane is moved slightly away from the aperture, the image of aperture is still recognizable but the fringes become prominent. This phenomenon is known as Fresnel or near-field diffraction. The Fresnel Approximation is a simplified version of the Huygens-Fresnel principle, and it is used to predict the near-field diffraction. The Fresnel diffraction formula is

$$E(x,y) = \frac{e^{ikz}}{i\lambda z} e^{i\frac{k}{2z}(x^2+y^2)} \iint_{-\infty}^{\infty} \left\{E(\xi,\eta) e^{i\frac{k}{2z}(\xi^2+\eta^2)}\right\} e^{-i\frac{k}{2z}(x\xi+y\eta)} d\xi d\eta, \tag{3.17}$$

which is the Fourier transform of the product of the complex field and a quadratic phase exponential. This approximation is valid with small k_x and k_y, therefore Fresnel approximation is a small-angle approximation. It is valid if the distance z satisfies

$$z \gg \frac{\pi}{4\lambda}[(x-\xi)^2+(y-\eta)^2]^2_{max}, \tag{3.18}$$

When the observing plane is moved further away from the aperture, a continuous change in fringes results. The image of the aperture cannot be resembled from the diffraction pattern anymore. Moving even further away from the aperture can only influence the size but not the shape of the diffraction anymore. This is known as Fraunhofer or far-field diffraction. If in addition to the Fresnel approximation the stricter (Fraunhofer) approximation

$$z \gg \frac{k(\xi^2+\eta^2)_{max}}{2}, \tag{3.19}$$

is satisfied, then the quadratic phase factor in Eq. (3.17) is approximately unity over the entire aperture and the observed electric field can be directly obtained by a Fourier transform of the aperture distribution itself. Therefore, the Fraunhofer diffraction is stated as

$$E(x,y) = \frac{e^{ikz}}{i\lambda z} e^{i\frac{k}{2z}(x^2+y^2)} \iint_{-\infty}^{\infty} E(\xi,\eta)\, \mathrm{e}^{-i\frac{k}{2z}(x\xi+y\eta)} d\xi d\eta. \tag{3.20}$$

In order to estimate which propagation approach is applicable to calculate a diffraction, the Fresnel number is used, defined as

$$F = \frac{a^2}{L\lambda}, \tag{3.21}$$

where a is the size of the objects, L is the propagation distance and λ is the wavelength of the wave.

For $F \gg 1$, the correct approximation for the near-field propagation is the angular spectrum method.

For $F \sim 1$, the correct approximation for the near-field propagation is Fresnel diffraction.

For $F \ll 1$, the propagation distance is much larger than the size of the apertures. The propagation is well described by Fraunhofer diffraction.

The diffraction grating

In principle, a repetitive array of diffracting elements, either apertures or obstacles, that has the effect of producing periodic alterations in the phase, amplitude or both of an emergent wave is said to be a diffraction grating. A wavefront when passing through such a system (e.g. multi-slit) is confronted by altering opaque and transparent regions,

so that it undergoes a modulation in amplitude, and such a configuration is called transmission amplitude grating. Another common form of transmission grating is made by ruling or scratching parallel notches into the surface of a flat, clear glass plate. Each of the scratches serves as a source of scattered light and together they form a regular array of parallel line sources. When the amplitude modulation from each point source are negligible, the variation in the optical thickness of propagation across the grating yield a phase modulation, and such configuration is known as transmission phase grating.

A transmission phase grating is defined by a few parameters, which are pitch size Λ and duty cycle $\frac{r}{\Lambda}$, as shown in Figure 3.1. With a normal incidence on a grating, the diffraction pattern in the far-field is well defined by Fraunhofer diffraction, and it is followed by

$$a\ sin\theta_m = m\lambda\ , \tag{3.22}$$

which is known as grating equation. a is the refractive index of the media through which waves propagate. The values of m specify the order of the various principle maxima.

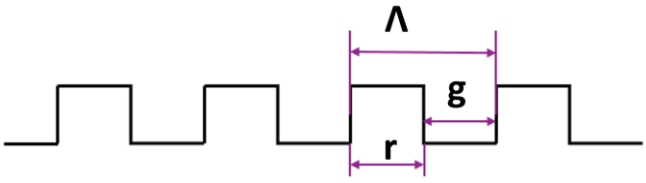

Figure 3.1 Schematic diagram of rectangular grating structure. Λ is the pitch size, g is the width of grooves, and r is the width of ridges.

3.1.3 Gaussian beam

In optics, a gaussian beam has an ideally Gaussian flux intensity over the beam's cross section. It is described by the lowest order or transverse mode TEM00, which is the most widely used due to that it is completely spatial coherence.

The mathematical description of a Gaussian beam is given by,

$$E(r,z) = E_0\hat{x}\frac{w_0}{w(z)}\exp\left(-\frac{r^2}{w(z)^2}\right)\exp\left(-i\left(kz + k\frac{r^2}{2R(z)} - \psi(z)\right)\right), \tag{3.23}$$

where r is the radial distance from the center axis of the beam,

z is the axial distance from the beam's focus,

i is the imaginary unit,

$k = \frac{2\pi n}{\lambda}$ is the wave vector for a free space wavelength λ and n is the refractive index in the media,

$E_0 = E(0,0)$ is the electric field amplitude and phase at the origin at time 0,

$w(z)$ is the radius at which the field amplitude falls of $\frac{1}{e}$ of their axial values, at the plane z along the beam.
$w_0 = w(0)$ is the beam waist radius,
$R(z)$ is the radius of curvature of the beam's wave front at z, and
$\psi(z)$ is the Gouy phase at z, an extra phase term beyond that attribute to the phase velocity of light.

Conveniently speaking, there are few parameters defining a Gaussian beam. They are beam waist w_0, Rayleigh range z_R and beam divergence θ.

Beam waist is the beam width at its focus where the beam width $w(z)$ is the smallest. Beam width is given by

$$w(z) = w_0\sqrt{1 + \left(\frac{z}{z_R}\right)^2}, \tag{3.24}$$

where

$$z_R = \frac{\pi w_0^2 n}{\lambda}, \tag{3.25}$$

is called the Rayleigh range. At Rayleigh range, the beam width $w(z)$ is $\sqrt{2}$ larger than it is at focus w_0. At a distance of z_R from focus, the wavefront curvature is the greatest as well.

Beam divergence is defined as

$$\theta \sim \frac{Aperture\ size}{2 \cdot Focal\ length}, \tag{3.26}$$

$$\theta \simeq \frac{\lambda}{\pi n w_0}, \tag{3.27}$$

where the aperture size is the beam diameters at the infinite distance from focus.

In this experiment, the beam diameters $w(z)$ is defined as the radius at which the field amplitude falls of 1/e of their axial values, at the plane z along the beam. The beam size in radius w_0 at focus is calculated based on Eq.(3.26) and Eq.(3.27). Aperture size is directly measured by iris size and focal length varies bases on the spherical mirror used in the experiment. The peak intensity of the beam is determined by

$$I = \frac{P}{repetition\ rate\ of\ laser * pulses\ duration * w_0}, \tag{3.28}$$

where P is the power of input beam measured by powermeter.

3.2 Experimental methods

This section describes the essential information to understand the experiments. It consists of the following parts. 1) Laser system. 2) Experimental setup, including optical paths, generation chamber and detection chamber. 3)Frequency resolved optical gating.

3.2.1 Laser system

The experiments were performed with an Astrella, a laser system designed and created by Coherent Inc. An Astrella is a Titanium: Sapphire diode-laser-pumped chirped pulse amplifier (CPA), operating at 1 kHz repetition rate with a central wavelength of 800 nm, a pulse energy of 7 mJ, and a pulse duration of around 35 fs (ideally). It starts with a seed laser (Vitara oscillator) producing femtosecond infrared pulses with a repetition rate of 80 MHz, then the pulses are stretched and sent to a regenerative amplifier (pumped by a Revolution pump laser) where 1 in 80,000 pulses is amplified. Afterwards the pulses are compressed to 800 nm, 1kHz, 35 fs, 7 mJ.

3.2.2 Experimental setup

To examine the specifics of highly nonlinear radiation from structured solids, experiments were carried out with femtosecond laser pulses interacting with different structured samples. The optical path was constant for all measurements. The generation schemes and detection schemes vary with different samples. Figure 3.2 shows a general experimental setup for solid-state HHG, hereafter called the "conventional setup". The generation and detection scheme will be explained subsequently with detailed diagrams.

Conventional setup

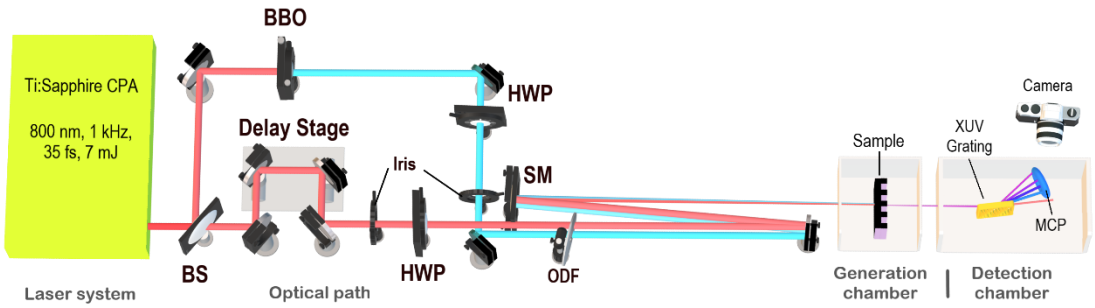

Figure 3.2 Diagram of the experimental setup and conventional generation scheme (unmarked optics are flat mirrors). BS: beam splitter, BBO: Barium borate crystal, HWP: half-wave plate, ODF: optical density filter, SM: spherical mirror, MCP: micro-channel plate. Optical path has a main arm (bottom) of 800nm pulses with a delay stage and a side arm (top) of 400 nm pulses.

Figure 3.2 shows the conventional experimental setup for solid-state HHG. Femtosecond infrared pulses are generated by the Astrella with a power of 7 W before the pulses are split into two different optical arms by a beam splitter (BS). The two optical arms are designed to accomplish experiments with the incidence of different wavelengths. The main arm (bottom arm) guides pulses with a central wavelength of 800 nm, and side arm (top arm) guides pulses with a central wavelength of 400 nm. The 400 nm is generated by a Barium borate crystal, abbreviated as BBO, which is a common nonlinear optical crystal. Most measurements are carried out with only one beam path, while another beam path is blocked. The aperture and peak intensity of the beam are controlled by iris and optical density filters (ODF) respectively. The polarization of the beam from the Astrella is horizontally linearly polarized, after the BBO polarization of 400 nm is changed by 90°. The polarization is adjusted by two half-wave plates (HWP) with polarizers which are not shown in Figure 3.2. In the end, the beam is focused by a spherical mirror on samples from which high-harmonics are emitted. The different photon energies are dispersed by XUV diffraction grating and detected by a double-stacked micro-channel plate (MCP) backed with a phosphor screen. The spectra are averaged photos recorded by a CMOS camera.

Generation Schemes

Since structures are only fabricated on one side of the samples, there are two generation schemes shown in Figure 3.3. Configuration 1 is the unstructured side facing the incident beam and high-harmonics are emitted from the structured side while configuration 2 is the opposite as high-harmonics are generated from the flat surface.

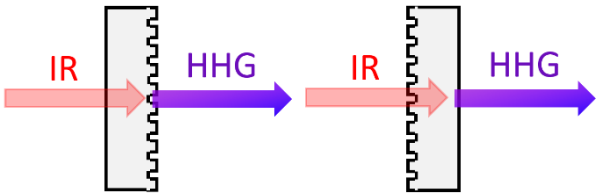

Figure 3.3 Generation schemes, (a)Configuration 1, (b)Configuration 2.

Detection Schemes

Due to the different structures of the samples and constraints of the experimental setup, there are three different detection schemes as illustrated below. In all schemes, the samples were placed on a stage where their position is adjustable. To simplify the diagram, the stage is excluded from diagrams, as well as vacuum flanges. The mirror in all schemes is to reflect the image of the MCP to the camera. The home-built setup consists of two connected vacuum chambers, the generation and detection chamber.

Both chambers are kept under vacuum at a base pressure of about 10^{-7} mbar. Both chambers are backed by a turbo pump each and a joint roughing pump.

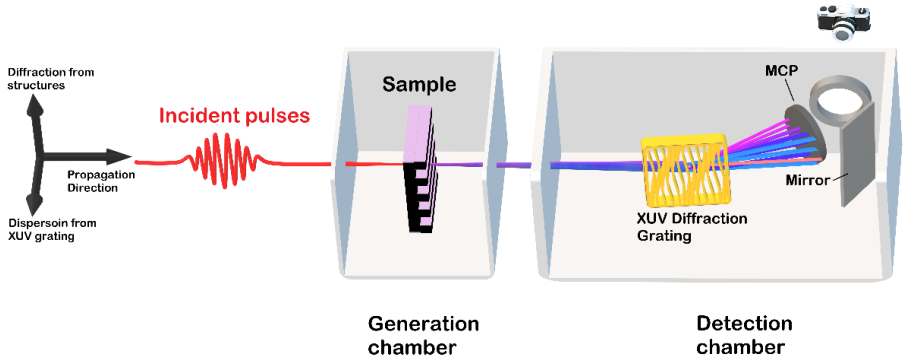

Figure 3.4 Diagram of detection scheme 1.

For grating samples with coarse structures (i.e. pitches >1μm, shown in section 3.3, Figure 3.11), the detection scheme is shown in Figure 3.4. The incident beam is focused on the samples, and high-harmonics along with the fundamental beam are propagated to the detection chamber through the flanges. Since the grating structures are aligned in such way that the grooves are horizontally oriented, diffraction is expected along the vertical direction. Different HHG orders are dispersed by an aberration-corrected flat-field concave XUV grating (Laminar-type Replica Diffraction Grating for Soft X-ray Region by Shimadzu, 1200 grooves/mm, model 30-002), the grating grooves of which are aligned vertically and thus 90° rotated with respect to the grooves of the generation sample.

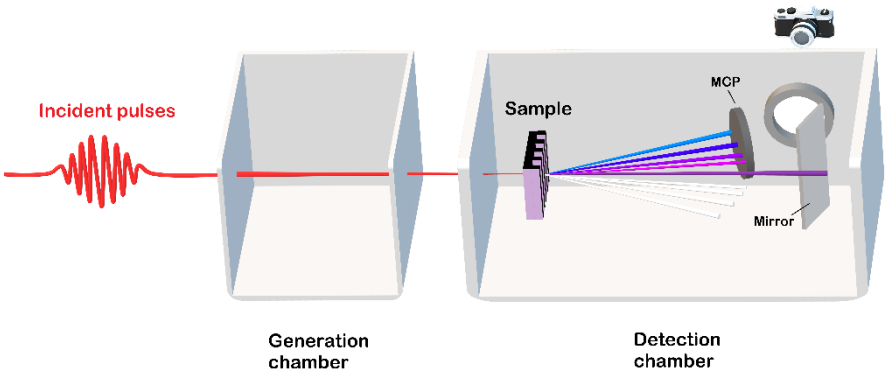

Figure 3.5 Diagram of detection scheme 2.

Figure 3.5 shows the detection scheme for the subwavelength grating structures (pitch size of 400 nm). The sample is set inside the detection chamber due to the large diffraction angle. The MCP is 30 cm away from the sample and offset off the central axis, so that the fundamental beam and 0^{th} order of the emitted radiation are blocked out, and the first order of the emitted XUV pulses is detected. The grooves of the subwavelength grating structures are aligned vertically, therefore diffraction is

expected on the horizontal plane. Only the first diffraction orders of HHG are captured by MCP. The 0^{th} and -1^{st} diffraction orders of HHG (marked as white) are excluded.

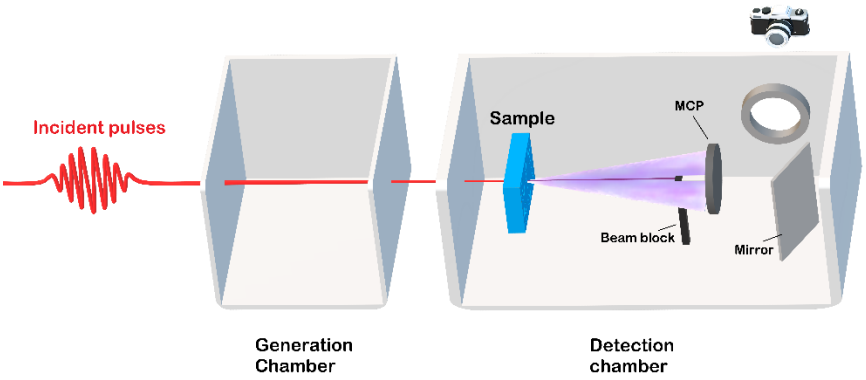

Figure 3.6 Diagram of detection scheme 3.

Figure 5 shows the detection scheme for the sample with complex patterns. The sample is placed inside the detection chamber with the MCP behind it. The fundamental beam is blocked by a beam block. The diffractions from all direction will be collected by the MCP.

3.2.3 Frequency-resolved optical gating

Frequency-resolved optical gating (FROG) is a reliable technique for completely characterizing spectral phase of an ultrashort laser pulse. Since its introduction in 1991 by Rick Trebino and Daniel J. Kane, FROG has evolved into a general and powerful technique for measuring ultrashort laser pulses. Ordinarily, to measure a short occasion, a shorter occasion is required but FROG tackled this problem by gating the laser pulse with itself to measure it. It is an autocorrelation-type measurement involving spectrum vs. time which gives the spectrogram mathematically described as

$$\Sigma_g(\omega,\tau) \equiv \left| \int_{-\infty}^{\infty} E(t)g(t-\tau)e^{-i\omega t}dt \right|^2, \qquad (3.29)$$

Instead of measuring an autocorrelator signal energy vs. delay, which yields a simple autocorrelation, FROG involves measuring the signal spectrum vs. delay. This extra dimension is the key to measuring pulses completely and without the need for assumptions.

In the FROG setup built in our lab, the second harmonic generation (SHG) FROG was used. By creating two replicas of the fundamental beam, a second harmonic signal can be obtained by focusing them on a nonlinear crystal (BBO). A spatial offset is introduced between two replicas, and the generated second harmonic signals is recorded, using a spectrometer, as a function of delay.

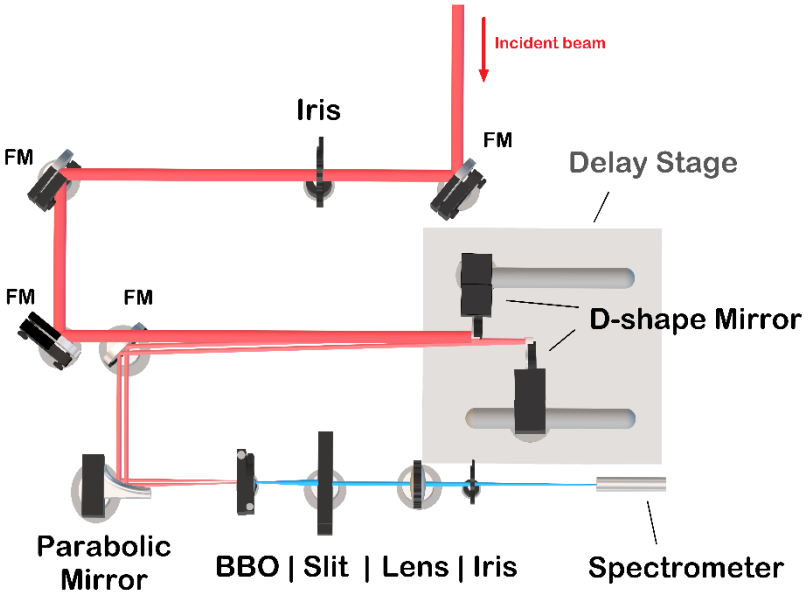

Figure 3.7 Diagram of FROG setup in the experiments. BBO: Barium borate crystal, FM: Flat mirror with Ag coating.

The FROG set-up built in the framework of this thesis to characterize the laser pulses is shown in Figure 3.7. The fundamental beam (infra-red pulses) is split by two D-shape mirrors (wavefront split) instead of by conventionally used beam spliter (amplitude split). A temporal delay is set by the translation stage (Thorlab Z825B) before they are focused by a parabolic mirror (10 cm focal length) into a BBO where the collinear SHG occurs. Eventually, SHG is selected by the slit and focused by a lens (5 cm focal length) to a spectrometer (OceanOptics USB2000PLUS FLMS12848). BBO has a phase match bandwidth which indicates a certain wavelength range of the fundamental beam for an efficient SHG occurring. A narrow phase matching bandwidth can cause a distortion on the spectral intensity profile, which may induce a big error when measuring short pulses. Phase matching bandwidth is related to the angle of BBO to the incidence, crystal orientation and the thickness of BBO. The thinner BBO is, the boarder phase matching bandwidth can be achieved. Eksma BBO has a thickness of 100 µm and designed for SHG with a central wavelength of 800 nm as the fundamental beam, which have a relative board bandwidth around 800 nm. The error induced by the BBO used in FROG setup is not a big concern. The spectrometer has a wavelength resolution of 0.45 nm, and it is embedded with an autocalibration for the transmission of the fiber and the wavelength dependent efficiency. A typical FROG trace is measured during experiments and shown in Figure 3.8. Since it is a SHG FROG, the measured wavelength is half of that of the fundamental beam. By using FROG, ultrafast pulses can be precisely characterized.

The incident pulses were characterized by SHG FROG shown in Figure 3.7. The original FROG trace was measured and shown in Figure 3.8. The reconstruction of spectrogram was accomplished using Femtosoft Technologies FROG 3.0 software.

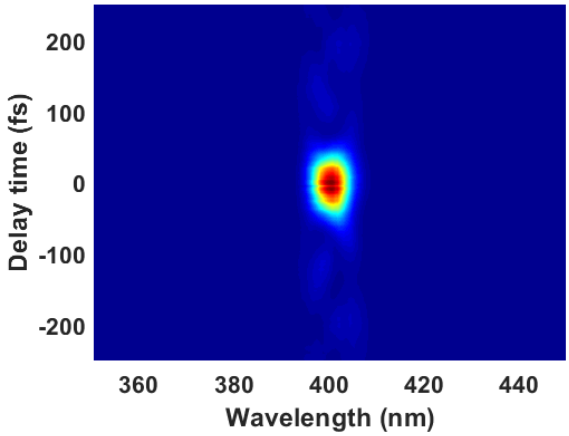

Figure 3.8 Measured FROG trace for the femtosecond pulses.

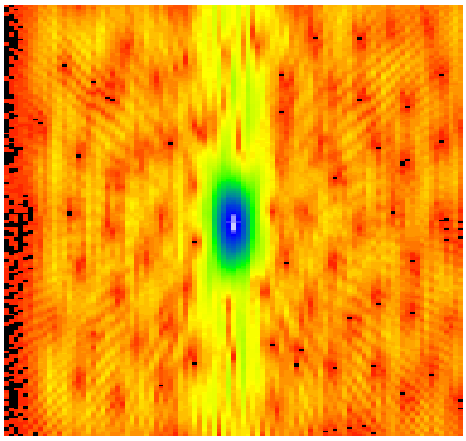

Figure 3.9 Retrieved FROG spectrogram from Femtosoft Technologies FROG 3.0 software.

It can be seen that the retrieved spectrogram has similar feature as measured FROG trace. Both shows a ‘horseshoe’ like shape which highlights the third order dispersion of pulses through media. The elongation of pulses could also caused by the dispersion when the pulses propagating through media. When the delay time is at 0, the pulse shows broader bandwidth than that at positive or negetive delay. That could be the self-modulation of pulses propagating through air. All these factors attribute to the elongation of the pulse duration than desired one (35 fs). Based on the temporal and spectral profile of characterised pulses. It indicates an Full witdh at half maximum (FWHM) of temporal shape of the pulse with around 50 fs, and FWHM bandwidth of spectral profile with around 30 nm. The fluctuation of temporal phase near central wavelength might caused by self-modulation, but it is mainly constant. The spectral phase shows an incease of phase with longer wavelength, indicating an negatively chirped feature.

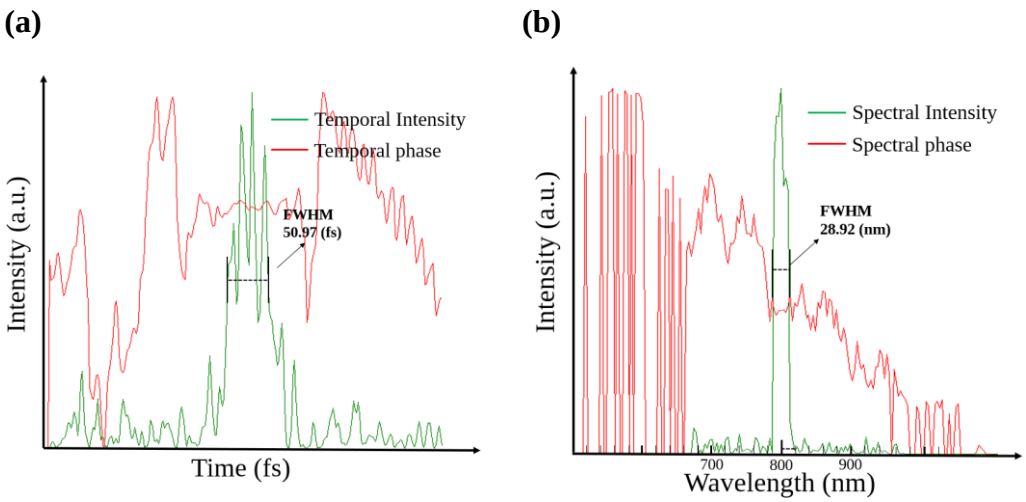

Figure 3.10 (a) Reconstructed temporal intensity vs. phase profile. The FWHM of temporal profile is 50.97 fs. (b) Reconstructed spectral intensity vs. phase profile. The FWHM of spectral profile is 28.92 nm.

3.3 Sample preparation and Characterization

Experiments are carried out on a 100 µm-thick fused silica substrate. Samples are fabricated by e-beam or UV lithography in an ISO class 5 cleanroom. Sample preparation follows the procedures described below.

First all substrates are cleaned following the base piranha procedure, then spin-coated with desired photoresist on the substrate by a SUSS Delta 80 Spin Coater. After a photoresist is applied on the substrate, a designed pattern is written in the photoresist layer by UV lithography (SUSS MA/BA 6 Mask Aligner) or E-Beam lithography (Raith e-LiNE lithography system Voyager), depending on the required pattern resolution. The pattern is transferred from the photoresist to a substrate by reactive ion etching using Oxford Plasmalab 80+ Ion Beam Etching. The final step is to lift-up photoresists.

3.3.1 General information

Samples

Substrates are thin fused silica slices with a diameter of 10 mm and a thickness of 0.1 mm. The substrates are supplied by UQG optics (Part No. CFS-1010). In this thesis, three different type of samples were produced by patterning the substrates. The first kind, the so called *grating sample*, is a sample having grating structures with a pitch size of 6 or 10 µm. The second kind, the so called *subwavelength sample*, is a sample with fine structures (400 µm pitch size). Even though the subwavelength sample has grating structures, to distinguish it from the first kind, it is called subwavelength sample. The third kind, the so called *patterned sample*, has a more complex structure.

Base Piranha

Base Piranha is 5:1:1 mixture of H_2O/30% NH_4OH/30% H_2O_2. The base piranha cleaning procedure follows these steps:

1. sonicate samples in distilled water for 10s in Branson 2800 Ultrasonic cleaning tank.
2. fill beaker with 50 ml H_2O and heat up to 75 to 80 deg.
3. add 10 ml 30% NH_4OH solution.
4. wait until temperature is back to 75 to 80 deg, add 10 ml 30% H_2O_2.
5. put sample in sample holder and put them in base piranha for 15 min.
6. rinse sample with distilled water before rinse with 2-propanol.

O_2 descum

O_2 descum is a cleaning procedure by bombarding the sample surface with O_2 to change the surface state and remove possible contaminations on the surface, and it is conducted in Oxford Plasmalab 80+ Ion Beam Etching. The cleaning parameters are 25 sccm of O_2 flow, 50 W of a forward power, 5 mTorr of pressure, 30 mTorr of strike pressure, and 20°C of operating temperature.

Acid Piranha

Acid Piranha is 5:1:1 mixture of H_2O/37% HCl/30% H_2O_2. The Acid Piranha follows the same steps as Base Piranha by replacing 30% NH_4OH with 37% HCl.

3.3.2 Grating Sample

The two grating samples are fabricated with UV lithography. They have a 6 µm pitch size and 33% duty cycle, and 10 µm pitch size and 50% duty cycle, respectively.

Sample preparation

Samples are cleaned following the based piranha and O2 descum procedures.

Spin-coating

For UV lithography, the Shipley microposit S1813 photoresist is used. S1813 is a positive photoresist with a dilute consistency. It is designed to spin-coat a thin layer of 1 to 2 µm. Spin coating parameters are shown in Table 1.

Table 1 Spin-coating parameters for S1813 photoresist.

Step	***Rotation [rpm]***	***Acceleration [rpm/s]***	***Time[s]***	***lid open (0) close (1)***	***Function***
1	*20*	*20*	*5*	*1*	*Close lid*
2	*1000*	*1000*	*45*	*1*	*Spin-coat S1813*
3	*0*	*1500*	*0*	*0*	*Stop spin*

UV-exposure

After obtaining a uniform photoresist layer, the sample is aligned on a SUSS MA/BA 6 UV Mask Aligner. The SUSS MA/BA 6 Mask Aligner has a pattern resolution around 1 μm by using 360 nm near ultraviolet light. The mask is designed using CleWin 3.2 Software and produced by the company DeltaMask (www.deltamask.nl).

The UV lithography exposure uses a Vacuum-Contact mode and the exposure time is 6.5 s.

Development

During development, the exposed part of a positive photoresist will remain and the unexposed photoresist resolves in the solution, which is called developer. Under a certain dose level, crosslinks in S1813 polymer chains are broken. The exposed area can be removed with the developer MF-319 (Rohm and Haas Electronic Materials LLC).

Samples are immersed in MF-319 developer for 45 s, then rinsed twice in distilled water for 15s separately.

Reactive-ion etching

The etching process is to help transfer the pattern from the photoresist to the substrates.

The SiO_2 etching has the following parameters: Ar flow of 25 sccm, CHF_3 flow of 25 sccm, pressure of 30 mTorr without strike pressure, forward power of 300 W and operating temperature of 20°C. Etching depth is 35-45 nm/min.

3.3.3 Subwavelength sample

Spin-coating

Since fused silica are poorly conducting substrates, different layers are needed to properly conduct e-beam lithography (EBL) on the sample. First, samples are cleaned by Base Piranha and O_2-descum to remove all contaminations, and then put on a hot-plate at 150° for 2 mins to remove residual water. Second, functional coatings or substances are applied layer-by-layer, as shown below, and the spin-coating parameters for the different layers are shown in Table 2.

1. HMDs (HexaMethylDiSilazan)
   HMDs is an adhesion layer to make photoresist attach to substrates.
   After the sample cooled down, apply HMDS to the surface and wait 10 s to form a monolayer. Then spin-coat the sample and transfer it to a hotplate at 150° for 1 min.
2. CSAR 62
   CSAR 62, also known as AR-P 6200, is a high-resolution photoresist for E-beam lithography.

Cool down the sample. Apply CSAR 62 with a pipette to cover two-thirds of the area of the substrate, then spin-coat the sample and bake the CSAR-coated sample on the hotplate at 150° for 2 mins.

3. Elektra 92

   Elektra is polythiophene based charge dissipation layer (AR-PC 5090.2). It is a conductive protective coating which gives a layer of 30 to 80 nm.

   Electra 92 is a conduction polymer that prevents charging of the surface during EBL. Cool down the sample. Apply Elektra 92 from the syringe, and spin-coat the sample, then place the sample on a hot plate for 90° for 2 mins.

4. Au Colloids

   This step is to creating focus points to help electrons focus on the sample for EBL.

   Deposit tiny droplets of 50nm Au colloids in 3 corners of the substrate and bake at 90° until the solution vaporized.

Table 2 Spin-coating parameters for different materials.

Materials	***Rotation [rpm]***	***Acceleration [rpm/s]***	***Time[s]***	***lid open (0) close (1)***
HMDs	*4000*	*1000*	*35*	*1/0*
CSAR 62	*4000*	*1000*	*45*	*0*
Elektra 92	*2000*	*1000*	*60*	*0*

E-beam lithography

After applying a suitable photoresist layer to the samples, they are ready to be exposed to electrons by the Raith e-LiNE lithography system Voyage. Due to the scattered electrons inside the samples, the dose level varies depending on the resolution of the patterns. The dose level used for subwavelength samples and complex patterns are 122.5 $\mu C \cdot cm^{-2}$ and 130 $\mu C \cdot cm^{-2}$ respectively. In this operation system, three levers under the samples are used to level the samples. A slanted surface can lead to a distance difference from e-beam to sample, therefore further affecting the dose factor inhomogeneously. To avoid that, the whole pattern is decomposed into small parts, so the calibration of leveling the sample can be conducted in between.

Development

To remove the photoresists and other materials, samples are immersed in pentyl acetate for 5 s, which dissolves most of the photoresist CSAR layer. The residue CSAR is further removed by putting samples in o-xylene for 5 s, before rinsing off the pentyl acetate from the first step by submerging the samples in a 9:1 mixture of MBIK/IPA solution for 15 s. In the end, the organic compounds are removed by IPA.

Reactive-ion etching

Same as above.

3.3.4 Sample characterization

Samples are characterized by optical microscopy (Zeiss Axioskop2), surface profiler (KLA-Tencor stylus profiler P7), and atomic force microscopy (Bruker Dimension icon XR).

Grating samples

The grating sample with large pitch size was characterized by optical microscopy (Figure 3.11) and surface profilometer (Figure 3.12). The structure was only fabricated on the half area of the fused silica sample, while the other half was an unstructured sample. Since during the reactive ion etching, the edge of the grooves was not straightly etched down, the sample does not have perfectly rectangularly shaped grating. The first grating sample has a 10 µm pitch size, 50% duty cycle and a groove depth of 85 nm. The second grating sample has a 6 µm pitch size, 33% duty cycle and a groove depth of 105 nm.

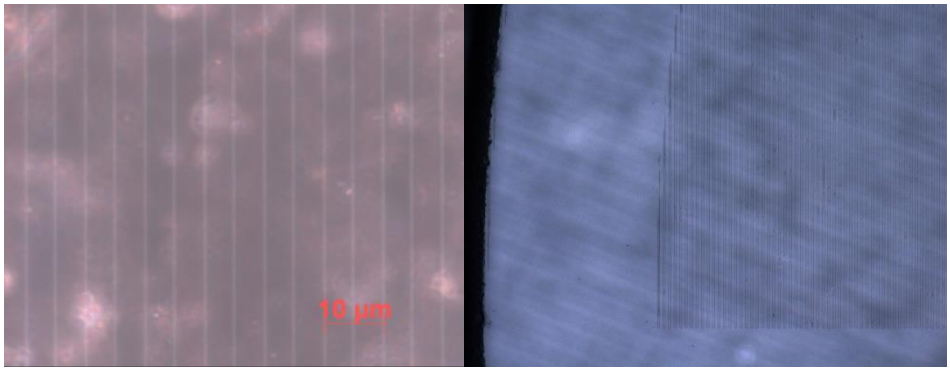

Figure 3.11 Optical microscopy image of 10 µm pitch size 50 % duty cycle grating structure on SiO_2 substrate. (Lines indicates edges of grooves.)

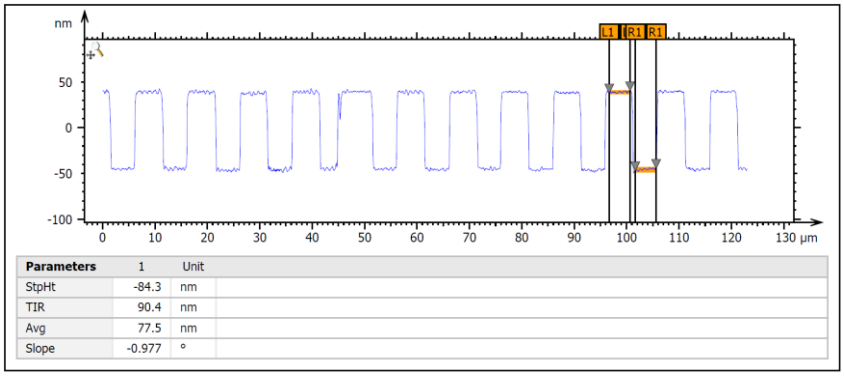

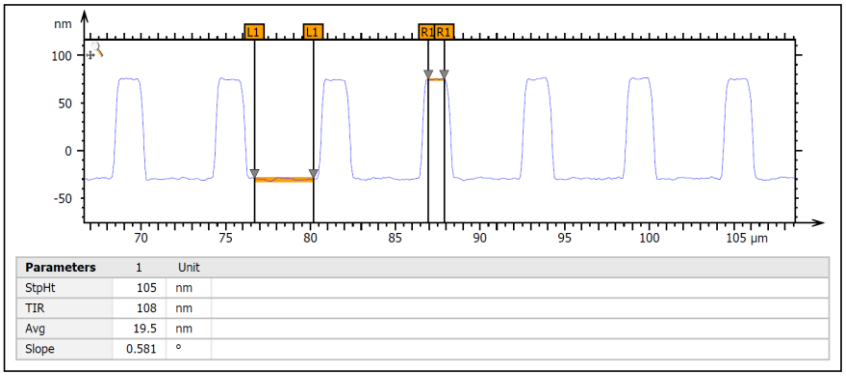

Figure 3.12 Sample characteristic from profilers of 10 µm pitch size 50 % duty cycle grating structure on SiO_2 substrate. Blue lines indicate the 2D profile of grating structures. 'StpHt' is the step height between selected range (indicating as orange lines) (L1, L1) and (R1, R1). In this case 'StpHt' is the groove depth of grating structure.

Subwavelength and patterned structures

Subwavelength and patterned structures were fabricated by EBL. The 3D profile of the subwavelength grating is shown in Figure 3.13. The subwavelength grating has 400 nm pitch size, 50% duty cycle and a groove depth of 87 nm. The complex patterns are shown in Figure 3.14, which consists of a smiley mark, a heart and a series of letters covering a square area of 200^2 μm^2. Dark lines sketch the contour of these features. Areas inside the loops were etched down by 87 nm.

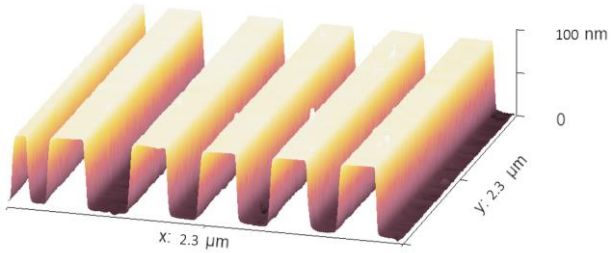

Figure 3.13 AFM image of subwavelength grating structure on SiO_2 substrate

Figure 3.14 Optical microscopy image of complex pattern on SiO_2 substrate.

4

Results and Discussions

In this chapter, the experimental results are presented, interpreted and linked to the motivation and aim of this project. The samples utilized to conduct experiments are shown in the previous chapter. For different experiments, the experimental setup is distinguished as 1, 2 and 3, based on the usage of the XUV diffraction grating, the sample position and the MCP position, which are shown in Figure 3.4 to Figure 3.6.

4.1 Control HHG spatial property

In this section, two different grating structures were used, which are 10 µm, 50% duty cycle and 6 µm, 33% duty cycle, respectively. The samples have a characteristic of large structures compared to the wavelength of the incident beam.

4.1.1 XUV spectrum from structured SiO2

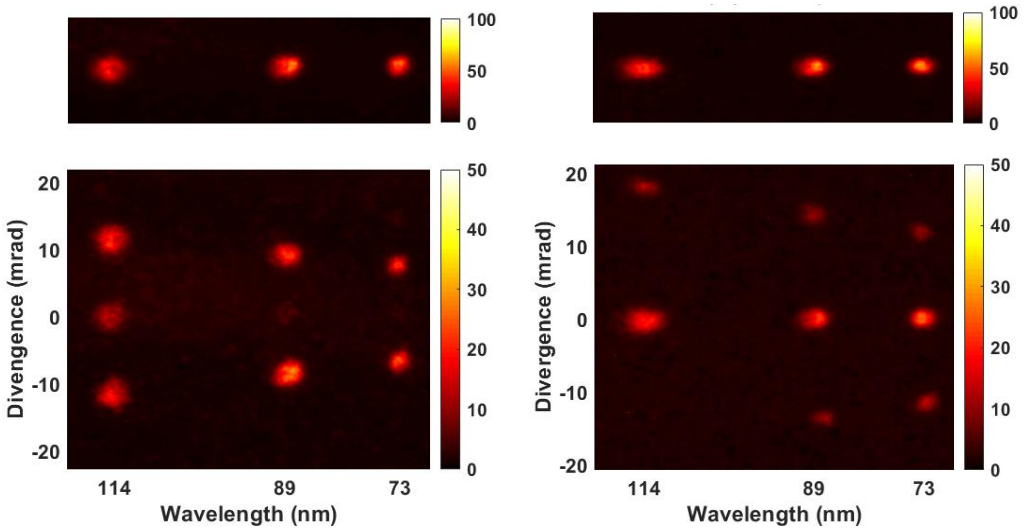

Figure 4.1 HHG spectrum from structured samples (setup 1 configuration 1). (a) Top spectrum from unstructured sample and bottom spectrum from 10 µm, 50% duty cycle grating, peak intensity is 1.5 TW/cm^2. (b) Top spectrum from unstructured sample and bottom spectrum from 6µm 33% duty cycle grating, peak intensity is 2.7 TW/cm^2.

Figure 4.1 illustrates the HHG spectrum when the high-harmonics were emitted from the structured surface (Figure 3.3(a)). The spectrum was obtained by averaging the images that were recorded by the CMOS camera with an integration time of 1 second.

The voltage of the MCP for the first measurement Figure 4.1(a) was 2.39kV/5.39kV. The voltage of the MCP for the second measurement in Figure 4.1(b) was 2.30kV/5.30kV. We focused infrared femtosecond laser pulses with a central wavelength of 800 nm onto two differently structured fused silica samples (100 µm thick) using a 75 cm focal length spherical mirror. The focal beam size was around 190 µm to 250 µm in diameter, and the peak intensity for the different measurements are indicated in the figures. The polarization of the incident beam was perpendicular to the grooves of the grating structures. The two grating structures have 10 µm, 50% duty cycle and 6 µm and 33% duty cycle, respectively. The depth of grooves is 87 nm for both structures.

The bottom and top panels in Figure 4.1 show high harmonics generated from both structured and unstructured samples under the same conditions, respectively. The color bar shows the intensity of the HHG signals. Photons with different energies were separated by a XUV diffraction grating along the horizontal axis and the diffraction light from the grating structures of the samples were distributed along the vertical axis. Only the 1^{st} and the -1^{st} diffraction orders were captured on the MCP screen since the physical field of view was limited by the experimental setup. The -1^{st} diffraction order (around -18 mrad) for the 7^{th} harmonic in Figure 4.1(b) was absent due to the limitations of the detection angle in the setup.

High harmonics up to 11^{th} order were observed for both the structured and unstructured samples. The HHG spectrum from the grating structures reflect the wavelength dependent diffraction angle, and the pattern of emitted high-harmonics are determined by the pitch sizes of the grating structures. The diffraction angles can be calculated based on the grating equation, and the experimental results agree with the calculations. For example, the diffraction angles of the 7^{th} order high harmonic are 11.4 mrad and 19 mrad based on the grating equation, when the pitch size is 10 µm and 6 µm respectively.

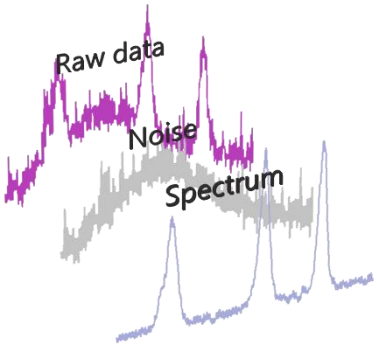

Figure 4.2 Illustration of background subtraction

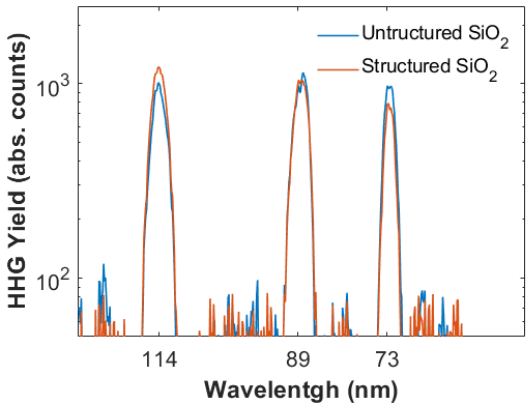

Figure 4.3 Comparison of HHG yield from structured and unstructured for 10 μm 50% duty cycle structure by integration counts over HHG signals. Spectrum was obtained when high-harmonics were generated on structured surface.

The diffraction efficiency varies for different photon energies and different grating structures, as the zeroth diffraction order of the 9th and 11th high-harmonics are barely present in Figure 4.1(a) but rather pronounced in Figure 4.1(b). The background noise was acquired as empty spectrum when there is no incidence going through sample. The noise is mainly attributed to the MCP reacting to the micro-particles in the chamber. It was subtracted and HHG spectrum after noise subtraction had a base line of a value fluctuating around 0 as shown in Figure 4.2. To compare HHG yields and enhancement, the intensity of the signal is calculated by integration of the pixel value around the signal area.

In this configuration, infrared pulses propagated through the unstructured surface and generated high harmonics on the grating structure. Compared to an incident beam on the structured surface and HHG from the unstructured surface, this configuration underlying Figure 4.1 does not provide an extra modulation for the IR pulses before they propagate to the back surface. Therefore, the harmonic yield is expected to be the same in both cases when experimental parameters are constant. The grating samples only impart phase differences onto harmonics generated from the top grooves (⊓) and bottom grooves (⊔), thus acting as a square transmission phase grating. Experimental result show that the HHG yield from bulk unstructured substrates and structured samples are the same as shown in Figure 4.3, which agrees with energy conservation in a traditional diffraction grating. With shorter wavelength, the diffraction efficiency decreases. That is the reason why there is a slight drop in yield ratio with higher harmonic order for emission from the structured sample (red spectrum in Figure 4.3) compared to the unstructured sample (blue spectrum in Figure 4.3).

The result shows that even though HHG is a nonlinear process, it follows the behavior of linear optics. The structured solid HHG exhibits great potential on modulating spatial properties of high harmonics during the generation process without extra optics.

4.1.2 Higher conversion efficiency of HHG from structured SiO_2

Due to the short attenuation length of HHG in fused silica, we conducted experiments in another configuration so that HHG are emitted from the unstructured surface.

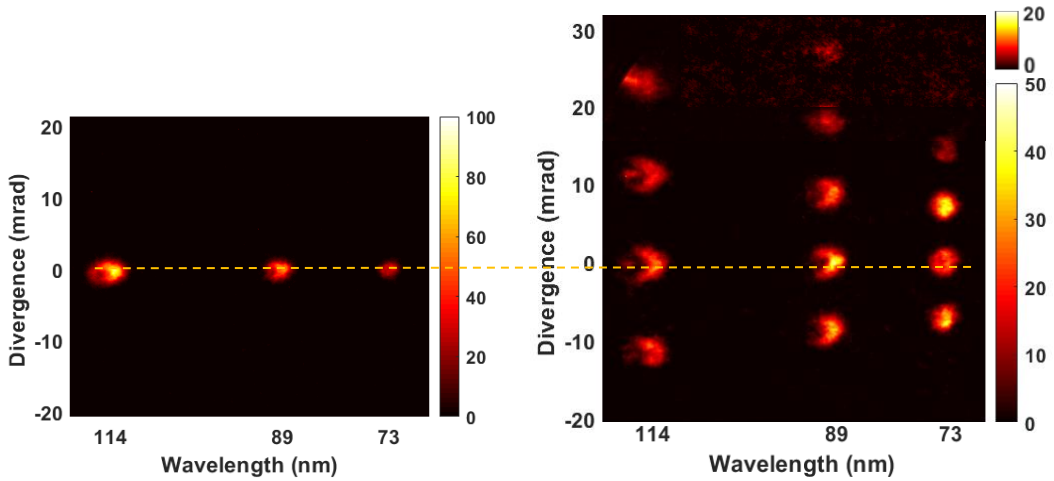

Figure 4.4 HHG spectrum from 10μm, 50% duty cycle grating (set-up 1, Figure 3.4, configuration 2, Figure 3.3(b)), peak intensity is 1.8 TW/cm^2. (a) Spectrum from unstructured sample, (b) spectrum from structured grating sample. The large range of divergence angles was obtained in a series of measurements changing the incident angle between infrared pulses and sample. Yellow dash line indicates the 0th diffraction order of HHG from the grating structure for both configurations.

Figure 4.4 illustrates the HHG spectrum when the infrared pulses were facing the structured surface and high-harmonics were emitted from the unstructured surface (Figure 3.3(b)). The spectrum was obtained by averaging the images recorded by a CMOS camera with an integration time of 1 second. The voltage of the MCP was 2.30 kV/5.30 kV. We focused infrared femtosecond laser pulses with a central wavelength of 800 nm onto structured Fused Silica (100 μm thick) using a 75 cm spherical mirror. The focal size was 290 μm in diameter, and the peak intensity is 1.8 TW/cm^2. The polarization of the incident beam was perpendicular to the grooves of the grating structures. The grating structure has 10 μm, 50% duty cycle with a depth of grooves of 87 nm.

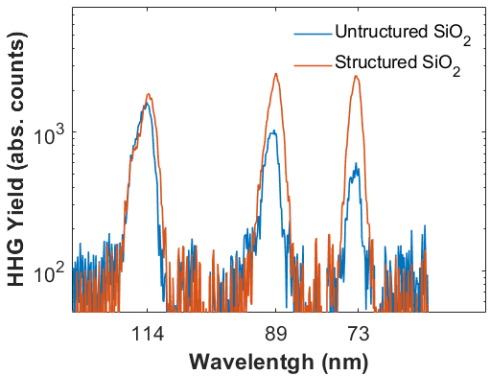

Figure 4.5 Comparison of HHG yield from structured and unstructured silica for 10 µm, 50% duty cycle structure by integrating the counts over the divergence axis. The spectrum was obtained when high-harmonics were generated on the flat surface.

In this configuration, the structured sample modulates the IR pulses and indirectly affects the high-harmonic-generation process. High harmonics up to the 11th order were observed in both configurations. Diffraction up to the 3rd order was captured by changing the incident angle between sample and infrared pulses. Figure 4.4(b) is the superposition of different spectra acquired under the same condition. For the +2nd diffraction order from the structures, the signal was weak, and thus plotted with a different color map as indicated on the side of the spectrum. Diffraction orders (±1st and 0th) from all wavelengths are firmly shown in the HHG spectrum and the intensity among these three diffraction orders is almost evenly distributed. The diffraction angles follow the grating equation and are the same as those resulting from the first configuration. It indicates that a grating-like structure with the same periodicity was successfully imprinted to the unstructured surface. Compared with the HHG spectrum obtained from the first configuration (Figure 4.1 (a)), the zeroth orders for the 9th and 11th high-harmonics have relatively high intensity. Moreover, the 2nd diffraction orders from structures were present, while they were absent in the first configuration. The absence of even diffraction orders is expected for 50% duty cycle gratings. This indicates that the diffraction of HHG in Fig. 4.4 is not directly related to the geometric factor of the grating structure on the sample. Comparing (a) and (b) in Figure 4.4, there is an enhancement of the relative signal compared to the harmonics yield on the unstructured sample, especially for the 11th harmonic order. The overall HHG yield from the structured sample is shown in Figure 4.5 by considering all diffraction orders.

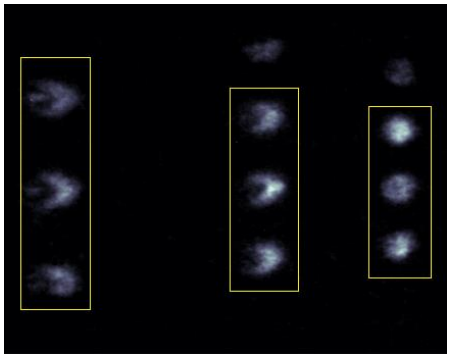

Figure 4.6 Illustration of comparison HHG enhancement for different wavelengths by the integration over only 1st and 0th diffraction orders

Since the higher diffraction orders were not present for all spectra, and most of the energy was conserved into the first and zeroth diffraction orders, only the ±1st and 0th were included to compare the relative yield of HHG between the structured and unstructured samples. Due to the presence of higher diffraction orders from structures, the HHG yield in this analysis is underestimated. To compare the HHG yield from the structured and unstructured sample, the yield ratio γ is defined as

$$\gamma^n = \frac{I^n_{+1st} + I^n_{0th} + I^n_{-1st}}{I^n_0}, \tag{4.1}$$

where n denotes the harmonic order, $+1^{st}$, 0^{th} and -1^{st} denote different diffraction orders, and I_0 denotes the intensity from the unstructured sample.

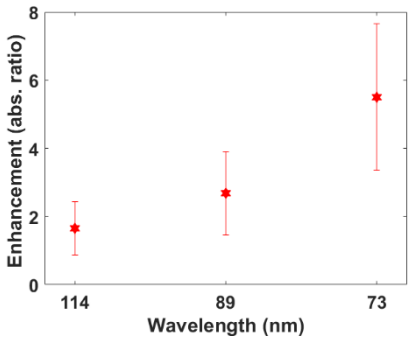

Figure 4.7 Enhancement on HHG yield of different wavelength when HHG are emitted from flat surface.

As illustrated in Figure 4.7, higher-order harmonics are more enhanced than lower-order harmonics. In this configuration, infrared pulses propagated through grating structures first and high harmonics were emitted from the unstructured surface. The structured sample acted as a transmission phase grating for IR pulses. With an aperture size of a few hundred micrometers (focal size) and a propagation distance of 100 μm (thickness of the substrate), the IR pulses were modulated following near-field propagation as the Fresnel number F≫1. The modulation on phase and amplitude of

the IR pulses may explain the enhancement of the HHG signals and the different HHG responses compared to high-harmonics generated from the structured surface.

From the experimental results, we successfully generated high-harmonics in an extreme ultraviolet regime and showed the control of HHG spatial properties. The diffraction patterns are observed in both configurations but showed different spatial properties. To further confirm what caused this difference, simulations were done to better understand the underlying physics.

4.1.3 Simulation

In this section, simulations based on diffraction theory are demonstrated. The simulations were done in MATLAB 2019R, and the study case is based on 10 μm, 50% duty cycle grating sample for both configurations (Figure 3.3(a)(b)). When the high-harmonics were generated from the structured surface, the sample acted as a transmission phase grating for HHG. Therefore, the phase difference for different wavelengths can be calculated based on the geometrical factor of the grating structures. When the high-harmonics were generated from the unstructured surface, the sample acted as transmission phase grating for IR. Therefore, the IR profile propagated to a flat surface, which can be obtained by numerical methods.

The simulation followed the following steps:

1. Generate a Gaussian beam profile of infrared.
2. Generate the profile of grating structure.
3. Propagate incident Gaussian beam through grating structure.
4. Obtain HHG near-field profile.
5. Propagate High-harmonic to far-field.

The Gaussian beam profile are generated based on Eq.(3.23) The focal length in the experiment was 75 cm and iris sizes were set to a few millimeters. The beam waist w_0 can be calculated using Eq. (3.26) and Eq. (3.27).Beam waist has an influence on the number of lines illuminated.

The simulation result shows that when the number of illuminated lines is sufficiently large, it does not play a critical role on the simulation result anymore. During the experiments, the iris size was 4 mm – 6 mm leading to a beam waist in radius of 75 μm – 130 μm. Therefore, a beam waist in radius of 100 μm was chosen in the simulation. For simplicity, the self-phase modulation of the incident beam during propagation in the optical path and in the sample are not taken into consideration. It is assumed that the high harmonics are generated at the focus of the incident beam and the incident beam is considered as a perfect Gaussian at focus.

A Gaussian beam of infrared light at the focal point is generated in MATLAB as shown in Figure 4.8. Brightness indicates the intensity of the beam and the color bar indicates the relative phase of the beam.

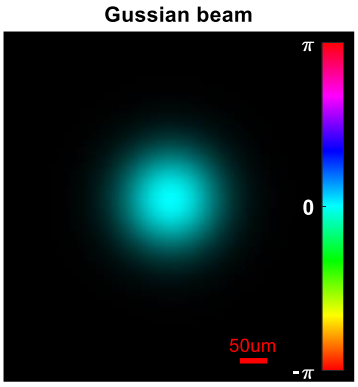

Figure 4.8 Simulated Gussian beam profile at focus (color bar indicates temporal phase of beam).

To create a grating structure, the grating structured is generated in MATLAB (code shown in Appendix) by generating a periodical structure with 10 μm as a repeat unit. Within every repeat unit, there are 20 pixels to ensure the precision of results.

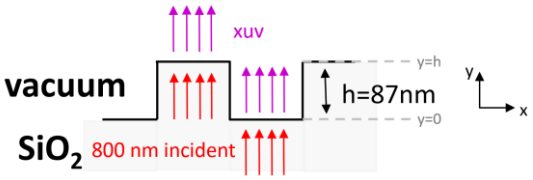

Figure 4.9 Scheme of high-harmonic generation when XUV is emitted from the structured surface (Configuration 1).

In Figure 4.9, the high-harmonic generation process in configuration 1 is illustrated. The phase difference for XUV introduced by structures is related to the IR phase before XUV are emitted from the surface. If the IR phase when it arrives at the plane of the bottom grooves (where y=0) $\varphi_{IR,0}$ is set to be 0, then $\varphi_{xuv,0}$ is also set to be 0 since $\varphi_{IR} = q \cdot \varphi_{xuv}$ where q is the order of the high-harmonics. The phase difference can be calculated by kL , where k is the wave vector and L is the propagated distance. The phase of XUV and IR reach the plane of the top grooves (y=h) are $\varphi_{xuv,h} = \frac{2\pi}{\lambda_{xuv}} h$ and $\varphi_{IR,h} = n_{IR} \frac{2\pi}{\lambda_{IR}} h$.

Therefore,

$$\varphi_{xuv,\sqcup} = \varphi_{xuv,h} - \varphi_{xuv,0} + \varphi_{abs} = \frac{2\pi}{\lambda_{xuv}} h + \varphi_{abs}, \quad (4.2)$$

and

$$\varphi_{xuv,\sqcup} = q \cdot \varphi_{IR,h} - \varphi_{xuv,0} + \varphi_{abs} = n_{IR} \frac{2\pi}{\lambda_{xuv}} h + \varphi_{abs}, \quad (4.3)$$

where φ_{abs} is an extra phase term within the attenuation length where IR is converted to XUV. The phase modulation for XUV in the first configuration can be calculated as

$$\Delta\varphi = \varphi_{xuv,\sqcup} - \varphi_{xuv,\sqcap} = \frac{2\pi h}{\lambda_{xuv}} (1 - n_{IR}), \quad (4.4)$$

where h, n_{IR}, λ_{xuv} are the groove depth, the refractive index of IR in fused silica and the wavelength of XUV respectively.

800 nm has a refractive index of 1.4608 in thin fused silica. The phase delay on the 7th, 9th and 11th harmonics are calculated as 0.7π, 0.9π and 1.1π respectively. The grating profile for the 11th high-harmonic is shown in Figure 4.10.

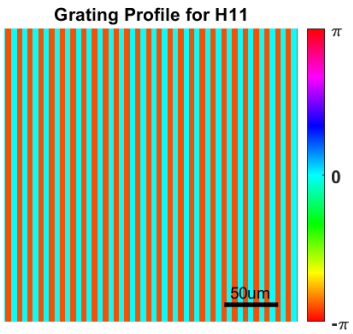

Figure 4.10 Grating structure for 11th high-harmonics when HHG emitted from structured surface (Configuration 1).

The near-field HHG beam profile (Figure 4.11) was obtained by multiplying the beam profile function with the grating function.

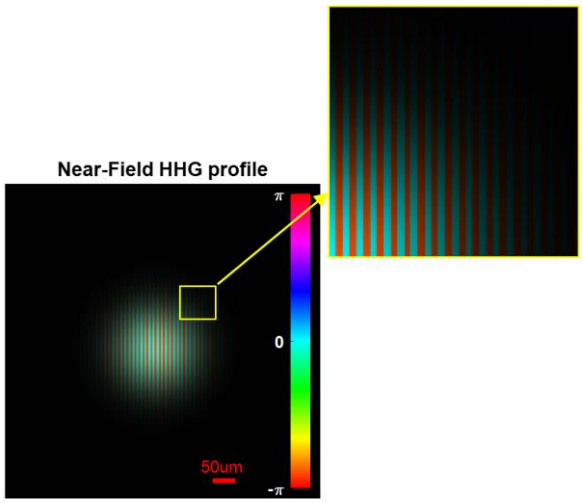

Figure 4.11 Near-field beam profile of 11th high-harmonic when HHG is emitted from structure surface (Configuration 1).

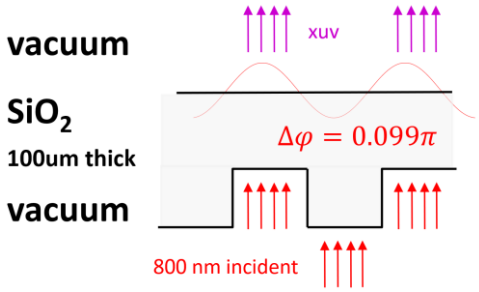

Figure 4.12 Scheme of high-harmonic generation when XUV emitted from flat surface (Configuration 2).

In Figure 4.12, the high-harmonic generation process in configuration 2 is illustrated. In the second configuration, the sample acts as a transmission phase grating for IR and this phase delay can be calculated as

$$\Delta\varphi = \varphi_{IR,\sqcup} - \varphi_{IR,\sqcap} = n_{IR}\frac{2\pi}{\lambda_{IR}}h\,. \tag{4.5}$$

The phase difference introduced by the structures is 0.099π for IR. A grating profile for IR is shown in Figure 4.13. By multiplying the beam function and the grating function for IR, a near-field IR profile can be obtained. The structure induced the phase and amplitude modulation on IR when it propagated to the flat surface where the high-harmonics were generated. Since the Fresnel number is much larger than 1, the Fresnel propagation operator was used to obtain the IR field at the flat surface.

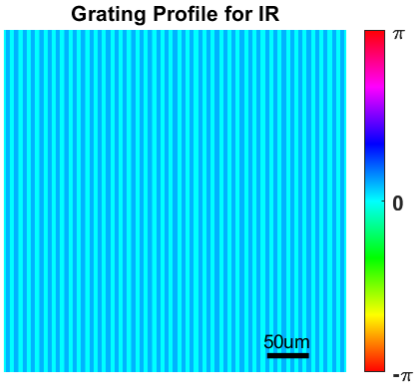

Figure 4.13 Grating profile of 10μm, 50% duty cycle and phase delay between ridges and grooves are calculated based on IR pulses as an example.

The IR field when it propagated to back surface is shown in Figure 4.14(a). The beam profile showed a sinusoidal-like periodic structure of both the amplitude and the phase. Compared to phase modulation of IR, amplitude modulation of IR played a more critical role. The intensity of the modulated IR beam along the horizontal direction is shown in Figure 4.14(b). It can be seen that the peak intensity increased by a factor of 1.2.

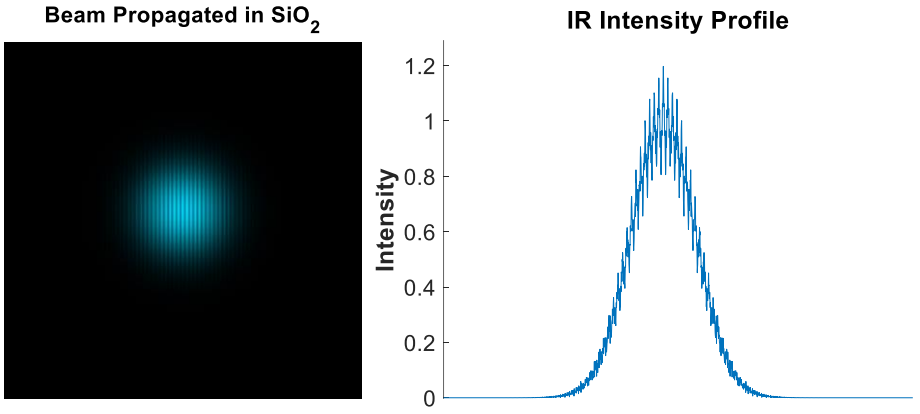

Figure 4.14 Beam profile of IR pulses at back surface of sample in configuration 2 after propagating inside the sample. (a) 2D Beam profile at back surface. (b) Normalised intensity modulation of beam along x central axis.

By knowing the electric field of fundamental IR beam profile, the near-field HHG profiles were converted to

$$\mathrm{H_q}(\mathrm{r},\varphi) \propto I_{IR}^{5} \cdot \mathrm{e}^{i \cdot q \cdot \varphi_{\mathrm{IR}}}, \tag{4.6}$$

where q is the high-harmonic order. It has been reported in gas-phase HHG that the phase of high harmonics has the following relation with the phase of fundamentals $\varphi_{hhg} = q \cdot \varphi_{IR}$. The peak intensity used in the experiments pushed the non-linearity close to a non-perturbative regime, which leads the intensity of high-harmonics to scale to I^5 as reported in some literatures. However, in reality the intensity of high-harmonics may scale between I^5 and I^q.

The near-field HHG profile for H7 is shown in Figure 4.15. Similar to other high-harmonic orders, near-field HHG profiles showed a clear sinusoidal intensity profile.

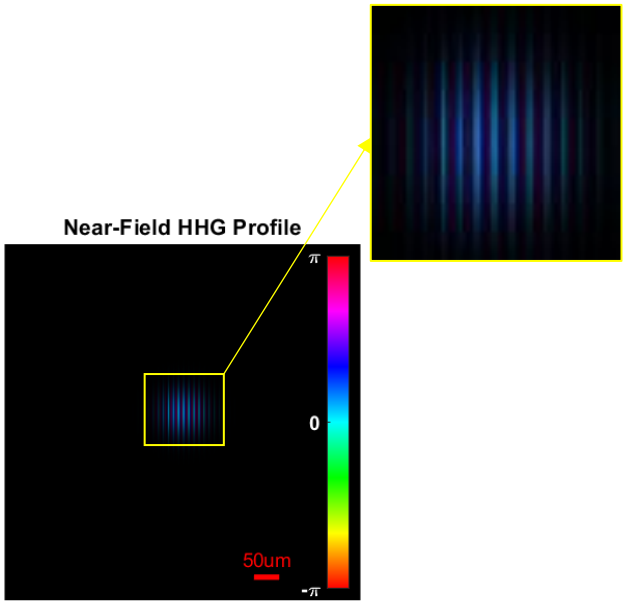

Figure 4.15 Near-field beam profile of 7th high-harmonic when HHG emitted from flat surface (Configuration 2).

The diffraction patterns of HHG were obtained using a Fresnel Propagator for every wavelength, then normalizing the diffraction angle to mrad and converting to one plot for both configurations. A simulated HHG spectrum for each configuration is shown in Figure 4.16. The simulation shows excellent agreement with the experimental results.

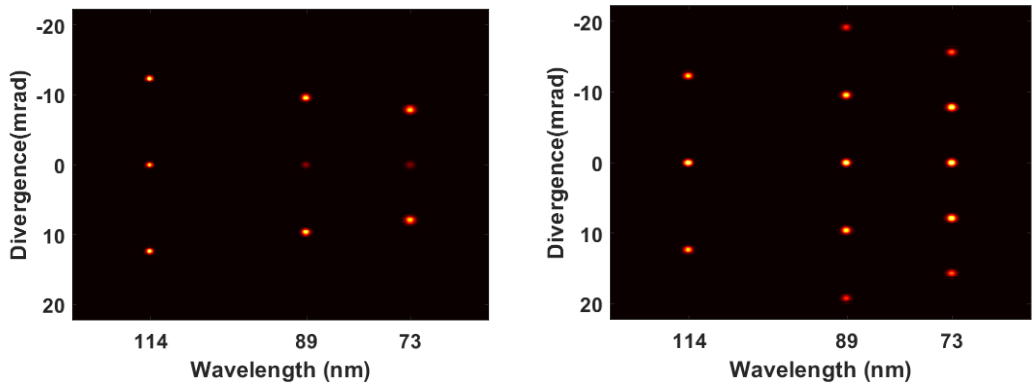

Figure 4.16 Simulation of HHG spectrum from 10μm, 50% duty cycle grating structures. (a) HHG from configuration 1, (Figure 3.3(a)). (b) HHG from configuration 2, (Figure 3.3(b)).

For the first configuration, the groove depth is comparable to the XUV wavelength, and thus the phase differences calculated for 7^{th}, 9^{th} and 11^{th} harmonics are 0.7π, 0.9π, 1.1π. That leads to destructive interference for the 0^{th} diffraction order which matches the experimental results. Due to the intrinsic properties of 50% duty cycle square transmission phase grating, even diffraction orders interfere destructively and are thus absent. This is shown in both simulation and experiments.

For the second configuration, the phase modulation of IR leads to a local peak enhancement of IR when it propagates to the flat surface. That explains the enhancement of the high-harmonic yield that was observed in experiments. A non-perturbative regime was considered in the simulation. However, the real situation must be the combination of tunneling and multiphoton absorption, so higher order harmonics may scale with a larger exponent than lower order harmonics. This may explain why the enhancement for higher order harmonics is more severe, which is not seen in the simulation. Meanwhile, the modulation of the IR transferred to HHG, leading to a sinusoidal phase and amplitude transmission grating for HHG. It explains diffraction pattern of XUV when it was generated from the flat surface and the different behavior than the XUV generated from the structured surface. In this case, even diffraction orders can be constructively built up as shown in both simulation and experiments.

4.1.4 Sample characterization after experiments

The sample was characterized under an optical microscope after the experiments. Figure 4.17 shows the front and back surface of the used sample. In some measurements, where the input laser peak intensity was above the damage threshold, the HHG signal decayed very fast due to the local damage on the sample. It produced grating-like damages on the flat surface. The material characterization after use shows that the damaged areas which have darker color, exhibit a periodicity of 10 μm. The line-structured damage indicates the inhomogeneity of the peak intensity. Along the

dark lines the local peak intensity is above the damage threshold of the bulk material while the peak intensity in the other areas is below the damage threshold. This damage only present on the sample locally, covering an area roughly around 6 mm^2.

This further confirmed that the near-field effect on the IR leads to an amplitude modulation, which was shown in the simulation section.

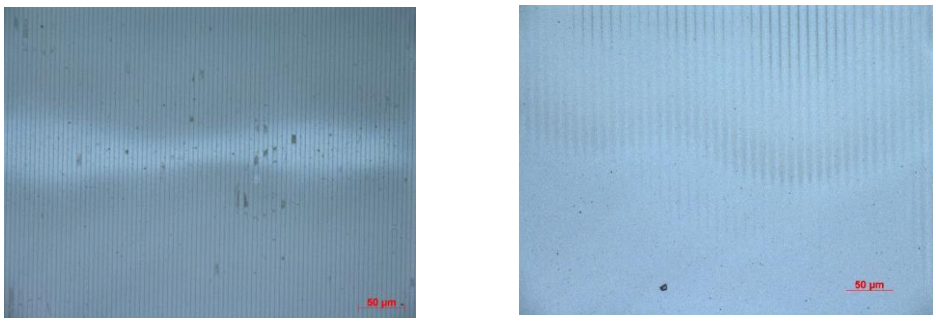

Figure 4.17 Characterization of the sample after experiments. (a) Structured surface. (b) Unstructured surface with optical damage.

4.1.5 Conclusion

From the above results, XUV radiation from structured fused silica is observed. By using grating structures, diffraction patterns were successfully obtained, and wavelength-dependent diffraction angles demonstrated a linear optical response of XUV from the geometric shape of solid structures. When high-harmonics were generated from the structured surface, samples acted as a transmission phase grating for XUV. The phase introduced from structures can be traced back and transferred from IR to XUV, and the agreement between experimental results and simulation results further proved that even though HHG is a non-linear process, at least for SiO_2, a structured surface alters the spatial properties of HHG in the XUV range following linear-optics rules. When high-harmonics were emitted from the unstructured surface, the similar diffraction pattern states the grating structure was imprinted onto the emission. Comparing the HHG spectra from both configurations exhibits the potential to modify the HHG profile directly through structures, or imprint the structures to the IR wave front and then indirectly control the HHG profile. Moreover, there is an enhancement of conversion efficiency based on the HHG spectrum when high-harmonics are emitted from an unstructured surface. This brings new insight to increase conversion efficiency without nanoantenna-like structures.

4.2 Extreme Ultraviolet High-harmonic Generation for Imaging

In this section, we investigate the possibility of applying XUV high-harmonics from solid state as an imaging tool. The samples used are subwavelength grating structures

and complex patterns. The measurement was conducted without XUV diffraction grating in the experimental setup (Figure 3.5).

4.2.1 Resolution of HHG imaging

The subwavelength grating has a pitch size of 400 nm and 50% duty cycle with a groove depth of 87 nm. Its structures are subwavelength in size compared to the wavelength of the incident beam of 800 nm. We focused infrared femtosecond laser pulses with a central wavelength of 800 nm and 400 nm onto structured Fused Silica (100 µm thick) using a 100 cm focal-length spherical mirror. The focal size was controlled by the iris size and the peak intensity for the different measurements are indicated in the figures. The polarization of the incident beam was parallel to the grooves of the grating structures.

In this experimental setup (Figure 3.5), the sample was put off-axis in front of the MCP at a distance of 30 cm. Therefore, only the $+1^{st}$ diffraction order from the subwavelength structures can be captured on the MCP. The MCP was horizontally displaced from the central axis by 6 cm so that only a diffraction pattern within 170 mrad to 270 mrad range could be detected. In principle, the first diffraction orders from the 5^{th} to 13^{th} high-harmonic orders were in the detection range. The calibration of photon energy was based on the grating equation Eq.(3.22), since from the above experiments we know high harmonics generated from grating structures follow linear optical rules when they are emitted from structured surface.

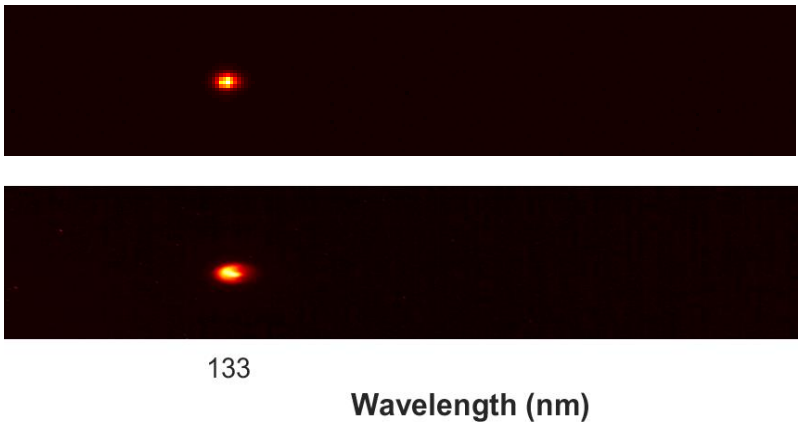

Figure 4.18 Spectrum of 1^{st} diffraction order of HHG from 400 nm pitch, 50% duty cycle grating structures. Incident beam is 400 nm with a peak intensity of 0.08 TW/cm^2. Above (a) HHG emitted from unstructured surface (Configuration 2). Bottom (b) HHG emitted from structured surface (Configuration 1).

In Figure 4.18, the spectrum shows the high-harmonic generation with incident pulses of 400 nm, 80 fs, 1kHz, 7mJ, when the high-harmonics were emitted from both the

unstructured (Figure 3.3(b) Configuration 2) and the structured surface (Figure 3.3(a) Configuration 1). The spectrum was obtained by averaging the images that were recorded by a CMOS camera with an integration time of 500 ms. The voltage of the MCP for the first measurement (Figure 4.18 (a)) was 2.0kV/5.0kV. The voltage of the MCP for the second measurement (Figure 4.18 (b)) was 1.95kV/4.95kV. The focal size was estimated as 130 µm in diameter. The peak intensity of the incident beam was 0.08 TW/cm^2.

Third-order harmonics from 400 nm pulses were observed in both configurations. Since the signal of the 3rd harmonic is extremely strong with increasing beam intensity, it saturated the MCP before that the peak intensity reaches the value which higher order harmonics are enable to generate. With such low peak intensity, this process was considered low-harmonic generation. However, a diffraction pattern can be observed in both configurations. The grating structure has a resolution of 400 nm which can be resolved by 400 nm light. The observation of the +1st diffraction order of the 3rd harmonic confirmed that the grating structures were imprinted onto the emission.

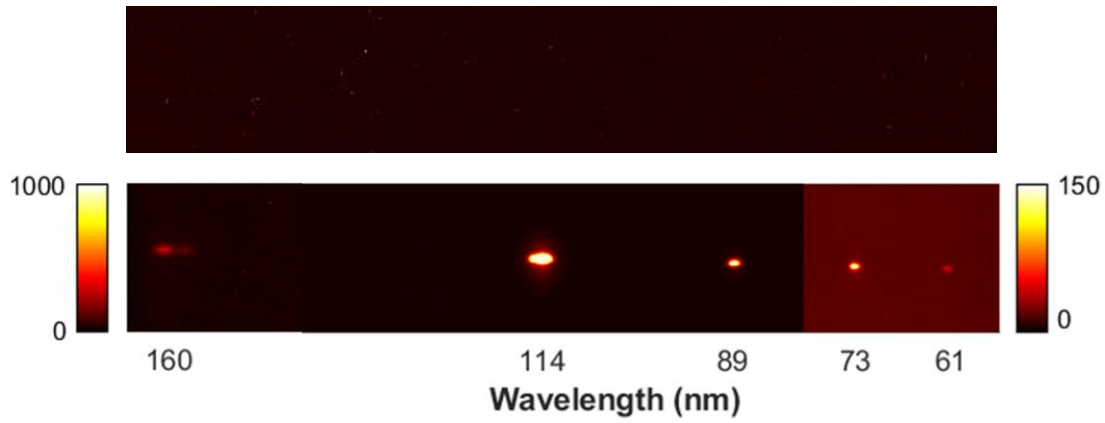

Figure 4.19 Spectrum of 1st diffraction order of HHG from 400 nm pitch 50% duty cycle grating structures. Incident beam is 800 nm with a peak intensity of 3.8 TW/cm^2. Above (a) HHG emitted from unstructured surface (Configuration 2). Bottom (b) HHG emitted from structured surface (Configuration 1).

In Figure 4.19, the spectrum shows high-harmonic generation with incident pulses of 800 nm, 80 fs, 1kHz, 7mJ, when the high-harmonics were emitted from both the unstructured (Configuration 2) and the structured surface (Configuration 1). The spectrum was obtained by averaging the images that were recorded by a CMOS camera with an integration time of 1 second. The voltage of the MCP was 2.15kV/5.15kV. The focal size was estimated as 250 µm in diameter. The peak intensity of the incident beam was 3.8 TW/cm^2.

When the high harmonics were generated from a flat surface, there was no diffraction signal recorded in the spectrum, see Figure 4.19 (a). Since the sample has fine structures smaller than 800 nm, 800 nm pulses became evanescencent wave when they

propagated through the structures. The small phase modulation on the wave front vanishes during propagation. Therefore, when the 800 nm pulses propagated to the flat surface where high-harmonics were emitted, they saw no structures and gave a Gaussian wave front – a flat wave front – at the focus. In this case, subwavelength structures are beyond the imaging resolution of the fundamental beam, thus the information cannot be carried by the fundamental beam and transferred to the HHG spectrum.

High-harmonics up to the 13^{th} order were observed when the high harmonics were generated from the structured surface, shown in Figure 4.19 (b). Structures induced a direct phase delay on XUV, and diffracted the XUV light since the structures were considered large features compared to the XUV wavelengths. By using solid state HHG, the imaging resolution is not limited by the resolution of the fundamental beam. The finest structure which is able to be resolved is determined by the wavelength of the high harmonics.

4.2.2 XUV HHG lens-less imaging for complex structures

From the above results, HHG showed the potential to achieve high spatial imaging by emitting short-wavelength XUV pulses. In this section, the diffraction patterns from a complex structure are investigated to further study the possibility of solid-state high-harmonic lens-less imaging. The complex pattern consists of a smiley mark with a heart and letters.

For lens-less imaging, the image of the object is obtained from far-field diffraction patterns by numerical methods. A diffraction pattern consisting of multiple wavelengths is always more trivial to reconstruct than one consisting of single wavelength. Therefore, the experiment first started with an incident beam of 400 nm only since the 3^{rd} harmonics of 400 nm overpowered all other signals (Figure 4.18) and the MCP has a weak response to low photon energy, such as 400 nm. In this case, the diffraction pattern from the samples can be considered as only consisting of one wavelength, namely 133 nm.

The diffraction patterns were simulated using MATLAB 2019R. The simulation is accomplished by multiplying a gaussian beam Eq.(3.23) with a phase terms that induced by the complex structure shown in Figure 3.14 (after rotating of 90°), before propagating to the observation plane using Fresnel propagator Eq.(3.17). The total pattern covers an area of 200 μm, which is similar to the Gaussian beam size in our experiments. Due to the intrinsic property of the Gaussian beam, not all illuminated parts will reach the peak intensity to generate high-harmonics, therefore, diffraction patterns were simulated for the three cases where the beam illuminates the whole pattern, only the smiley mark with a heart and only the letters, shown in Figure 4.20. It can be seen if only smiley mark is illuminated, the periodical fringe is very

prominent and it is attributed to the circle structure of the smiley mark (contour of the face and semicircle in the eyes and mouth). The dash line along x-axis is the characteristics of periodic grating-like structures from these curves or lines of face contour and eyes contour. When only letters are illuminated, the random strips are produced since the letters can be regarded as random line structures in both directions. It makes a multiple-slits structure with different spacings. All the characteristics are present but less prominent when the whole pattern is illuminated.

Based on the simulation, the experiment was set up as shown in Figure 3.6. The sample has been placed in front of the MCP with a distance of 30 cm. The fundamental beam (400 nm) was blocked after the sample by a metal rod with 2 mm width, so that the high intensity part could be filtered out and light could be recorded from diffraction. A few diffraction patterns were recorded shown in Figure 4.20(d)(e)(f). By colinearly arranging 400 nm with 800 nm as the incidence, a higher intensity can be achieved, and this diffraction pattern is displayed in Figure 4.21.

The similarity of the experimental and simulated diffraction patterns is pronounced. Even though the exact illuminated are is unknown, the acquired diffraction shows those characteristics from expected features on samples. Therefore, we suspect that the diffraction spectra shown in Figure 4.20(d)(e)(f) are corresponding to the simulation result in Figure 4.20(a)(b)(c) respectively. Since the dynamic range of the MCP is limited and the MCP has better response when detective light is perpendicular to it, the detective diffraction fades out with the increasing diffraction angle. The main features from the smiley marks and letters are still present in the experimental results. It is even more clear when using two colors, the outer line of diffraction patterns (Figure 4.21) shows double fringes as the simulation result of ‘smiley mark only’. The reconstruction of the object is required to complete the experiments.

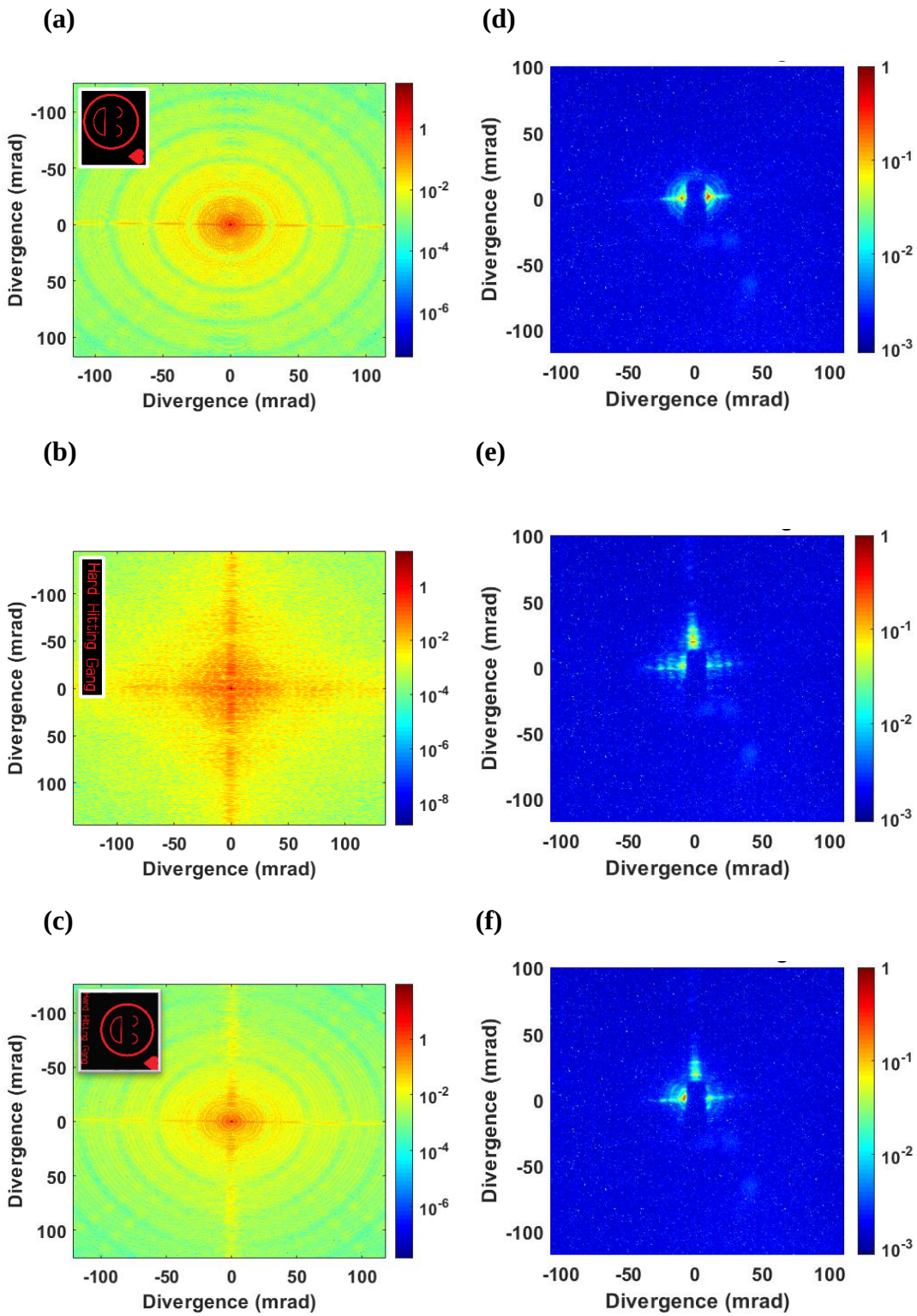

Figure 4.20 Left panel (a)~(c) is simulated diffraction patterns from 3rd harmonic of 400 nm by illuminated (a) smiley mark with a heart (b) only letters (c) smiley mark with letters. The insert images located in the up-left corner are the illuminated pattern. Right panel (d)~(f) is the experimental results by illuminated difference area of samples (3rd HHG from 400 nm incidence).

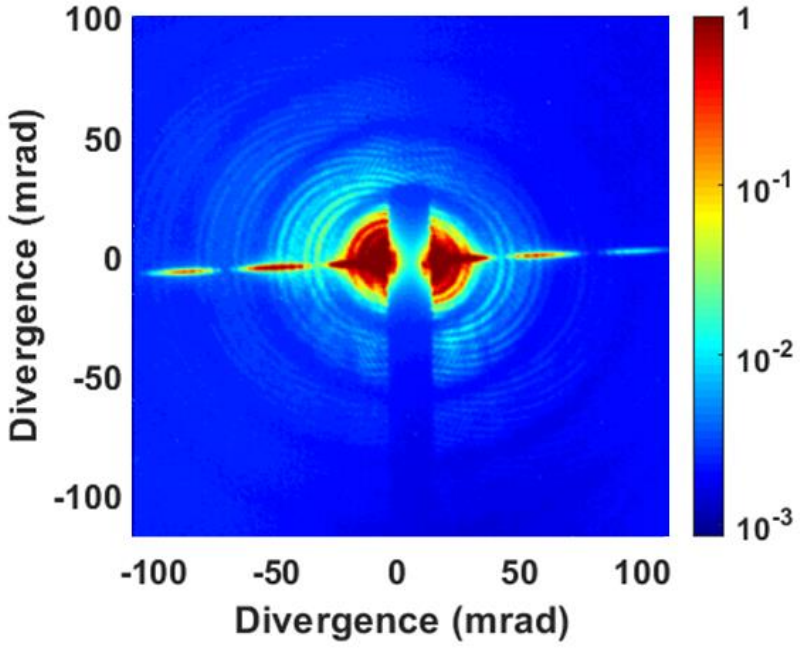

Figure 4.21 Diffraction patterns with collinear incident beam of 400 nm and 800 nm (mainly 3rd HHG from 400 nm).

4.2.3 Conclusion

The above results show the significant potential of HHG in lens-less imaging applications. By using subwavelength gratings, the results revealed that high-harmonic generation enables resolving finer structures which are beyond the resolution limits of the wavelength of the fundamental beams. When the imaging resolution is within the capability of the fundamental beam, structures can be resolved from both sides of the structures by a modulated fundamental profile or a modulated HHG profile. When the structures scale is smaller than the wavelength of the fundamental beam, meaning beyond the resolution of the fundamental beam, the structures are able to be resolved by shorter wavelength components – HHG. By using high-harmonic generation from solids, high-resolution by an intrinsic process on the materials itself was achieved, without damaging the sample. The diffraction patterns obtained from structures will be reconstructed by computational algorithm, which was beyond the scope of this thesis. This will make HHG from solids a promising tool for lens-less imaging. It enables fast imaging with high-resolution and does not require an incidence with short wavelength.

4.3 XUV in optical application

In previous experiments, XUV high-harmonic generation in the solid state successfully showed potential for changing the XUV high-harmonic spatial properties. By using subwavelength grating, different photon energies can be distinguished without utilization of an XUV diffraction grating. Moreover, higher HHG orders up to 13th are

detected (Figure 4.19) with even lower voltage of the MCP, which is not shown when using conventional detection scheme of HHG (Figure 3.4), due to a significant loss of signal from commercial XUV diffraction grating. Direct emission of HHG from fused silica subwavelength structures leads to separation of photon energies without a compromise of energy loss. In our experiments, only the first diffraction order was detected which leads to an overall even higher intensity of HHG if all diffraction orders were considered. With different grating designs, such as blazed grating, it is possible that nearly all generated high-harmonics converge to the first diffraction order. It brings new insights about applications on XUV optics by using high-harmonic generation from the solid state. Therefore, in this section, polarization dependent high-harmonic behaviors are demonstrated using subwavelength grating structures to further explore the possibility of XUV HHG from structured solids in optical applications.

The experimental setup for the polarization measurement is shown in Figure 3.5. In this experiment, the sample was set in configuration 2, shown in Figure 3.3 (a), and high harmonics are emitted from the structured surface. The first diffraction order from the subwavelength structures on the fused silica sample was detected by the MCP.

Figure 4.22 shows the polarization dependent intensity of high harmonics. The polarization at 0° indicates a polarization of the incidence parallel to the grooves. The polarization at 90° indicates a polarization of the incidence perpendicular to the grooves. With 800 nm incident pulses, the intensity is highly polarization dependent. The HHG intensity is at a minimum when the polarization is at 45°, and at a maximum at 90°. With 400 nm incident pulses, the intensity of HHG is not dependent on polarization (note that the fluctuation on the intensity of HHG from 400 nm is due to the different reflection efficiencies caused by the spherical mirror). It is well known that the birefringence effect emerges when the pitch size of a grating is much smaller than the incident beam. Practically, when the pitch size is smaller than 1/10 of the incidence wavelength, different polarizations can be separated in time due to different refractive indexes inside structures [56, 57, 58]. However, a similar effect was also found when the periodicity of the grating is only half of the wavelength of incidence. In a study by Kang et al. [59], the birefringence effect formed in fused silica grating with 119 nm pitch size under incidence of 193 nm light. This study is comparable with our experiment. It is highly possible that a birefringent effect is present in our study when incident pulses are 800 nm, even though the ratio between grating pitch size and wavelength is not << 1. The birefringent effect introduces different refractive indexes for different polarizations. Therefore, when the polarization is at 45°, the intensity can be resolved to two contributions. One is along 0° and the other is along 90°. Due to the nonlinearity of HHG, the overall intensity of HHG is weaker than that generated from one HHG source, while the total peak intensity remains the same.

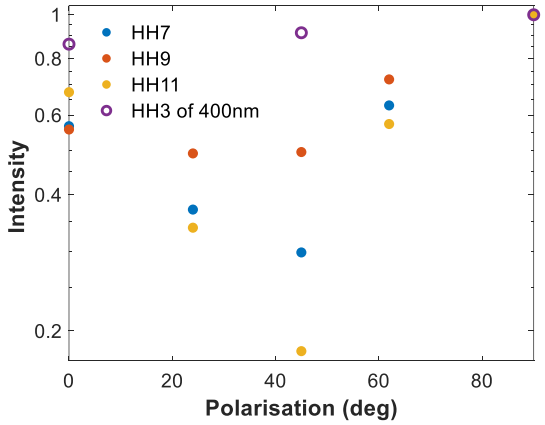

Figure 4.22 The intensity of the 7th, 9th and 11th harmonics of 800nm pulses and 3rd harmonics of 400nm pulses changing with the polarization of the incident beam.

In conclusion, XUV HHG from structured solids has great potential in XUV/EUV optics. Grating structures on dielectric materials are promising to be a new HHG source with high conversion efficiency. By choosing a reasonable shape and dimension of grating structures, photon energies can be separated with a certain angle and even lower photon energies can be filtered out if the dimension is sufficiently small. The polarization dependence result shows a formed birefringence effect on the fundamental beam, where high-harmonics were generated from two pulses with different polarization. It provides insight into the potential of using HHG from subwavelength grating structures as XUV/EUV polarizer or waveplate.

5

Conclusion

In this project, we have demonstrated extreme-ultraviolet high-harmonic generation from dielectric materials with designed structures. High-harmonics up to the 11^{th} order (73 nm) were observed when a 100 µm thin fused silica substrate (FS) was illuminated with infrared pulses with a central wavelength of 800 nm, a repetition rate of 1 kHz and a pulse duration of 80 fs. Higher photon energy (62 nm) were obtained with high-harmonics generated from grating structured FS. Using grating structures on fused silica, we successfully controlled the spatial properties of HHG. Considering the short attenuation length of HHG, only high harmonics emitted from the sample surfaces contributed to the overall signal. We investigated high-harmonic generation from both structured and unstructured surfaces. The wavelength dependent features can be predicted with the grating equation. Moreover, the far-field HHG profile can be retrieved from the phase and amplitude modulation of the near-field HHG profile and fundamental beam, which enable a precise control of the HHG profile. When high-harmonics were emitted from the structured side, a direct phase modulation was imposed on the HHG profile, leading to a diffraction. When emission occurred on the unstructured side, it yielded a modulation on the fundamental beam and imprinted the modulated profile of the fundamental beam into the emission, leading to an indirect control of the HHG profile. A higher conversion efficiency was observed as well from the latter case, without the use of previously proposed nanoantennas or plasmonic structures, which was mentioned in the literature. Our approach brings up the new concept of indirect control over HHG properties by shaping the fundamental beam from structured solids. It shows the potential of manipulating HHG profile with a higher conversion efficiency, and eliminates the possibility of fast deterioration of nanostructures.

As a crucial aspect of this project, we have shown a promising start of extreme-ultraviolet high-harmonic generation microscopy of solids. By illuminating subwavelength structures and complex patterns on FS, an emitted diffraction pattern was obtained from the structured FS. Images of objects can be further reconstructed from diffraction patterns if combined with a phase-retrieval algorithm, which will make HHG from solids a potential candidate for a fast imaging technique. The results indicated that the resolution of this technique is attributed to the wavelength of high-harmonics. With the intrinsic non-linear optical response of many materials (e.g. semiconductors and dielectrics) under a strong field, the resolution of HHG lens-less imaging could even reach a few nano-meters with long-wavelength incident light. The

fast optical response from the interaction between light and condensed matter enables this technique to image large objects within a short time frame. Apart from this, XUV HHG lens-less imaging is accomplished without damaging the materials, which may find application as a detection tool in the semiconductor or lithography industry.

In the end, we have investigated an essential prospective of high-harmonic generation in solids in terms of use in extreme-ultraviolet optics. The different high-harmonic orders can be distinguished using grating structures. It is possible to design the grating structure such that only one HHG order is selected and enhanced, which could be a potential HHG source for many other applications, such as time-resolved and angle-resolved photoelectron spectroscopy (trARPES). The result also showed that high-harmonic emission is sensitive to the polarization of the incident beam, which can be exploited to engineer the polarization of the high-harmonics. The birefringence effect deduced from subwavelength structures may open up a new branch of XUV optics for polarizers, waveplates etc.

6

Acknowledgement

During this one-year master graduation project, I gained more than I expected. First of all, I would like to thank my supervisor in ARCNL, Dr. Peter Kraus. Thanks for letting me join the group and giving me the opportunity to explore the field of optical physics. I really enjoyed a lot. You motivate me and guide me throughout the project. I am always amazed by how fast you can process all the information and came up with inspiring ideas. Then I would like to thank Prof. Marcel Sluiter, thank you for being my master supervisor and helping me dealing with all the issues. Even though this project is an external project, throughout my master program, you are being such an excellent teacher, and being patient and kind to all your students. I enjoyed your lectures very much.

Of course, this project would not have been accomplished without the guide of my daily supervisors, Sylvianne Roscam Abbing and Dr. Filippo Campi. Thank you for being so patient answering all my questions and teaching everything in the lab (plus foosball skill I learned ;p). Thank you for your trust as well. It was such a great time to work together. I wish one day I would reach your level in physics. Thank my other group members and everyone in ARCNL for creating an extremely nice working environment and being supportive to each other.

Thank my parents being supportive all the time and all my friends. Many loves.

References

[1] Corkum, Paul B, "Plasma perspective on strong field multiphoton ionization," *Physical review letters,* vol. 71, no. 13, p. 1994, 1993.

[2] Wörner, Hans Jakob, and Paul B. Corkum, "Attosecond spectroscopy," *Handbook of High-resolution Spectroscopy,* 2011.

[3] Harada, Tetsuo, et al., "Development of standalone coherent EUV scatterometry microscope with high-harmonic-generation EUV source," in *International Society for Optics and Photonics,* 2012.

[4] Sung, Hamin, et al., "Coherent EUV Light Source by High Harmonic Generation for EUV Metrology," *Recent Advances in Telecommunications and Circuits,* 2013.

[5] Jager, Marieke F., et al., "Tracking the insulator-to-metal phase transition in VO2 with few-femtosecond extreme UV transient absorption spectroscopy," *Proceedings of the National Academy of Sciences,* vol. 114, no. 36, pp. 9558-9563, 2017.

[6] Eich, Steffen, et al. , "Time-and angle-resolved photoemission spectroscopy with optimized high-harmonic pulses using frequency-doubled Ti: Sapphire lasers," *ournal of Electron Spectroscopy and Related Phenomena ,* vol. 195, pp. 231-236, 2014.

[7] Wörner, Hans Jakob, et al., "Following a chemical reaction using high-harmonic interferometry," *Nature,* vol. 466, no. 7306, pp. 604-607, 2010.

[8] Burnett, N. H., et al., "Harmonic generation in CO2 laser target interaction," *Applied Physics Letters,* vol. 31, no. 3, pp. 172-174, 31 3 1977.

[9] McPherson, A., et al., "Studies of multiphoton production of vacuum-ultraviolet radiation in the rare gases," *JOSA B,* vol. 4, no. 4, pp. 595-601, 1987.

[10] Eberly, J. H., Q. Su, and J. Javanainen. , "Nonlinear light scattering accompanying multiphoton ionization," *Physical review letters,* vol. 62, no. 8, p. 881, 1989.

[11] Li, X. F., et al., "Multiple-harmonic generation in rare gases at high laser intensity," *Physical Review A,* vol. 39, no. 11, p. 5751, 1989.

[12] Schafer, K. J., et al., "Above threshold ionization beyond the high harmonic cutoff," *Physical review letters,* vol. 70, no. 11, p. 1599, 1993.

[13] Lewenstein, Maciej, et al., "Theory of high-harmonic generation by low-frequency laser fields," *Physical Review A,* vol. 49, no. 3, p. 2117, 1994.

[14] Ghimire, Shambhu, et al., "Observation of high-order harmonic generation in a bulk crystal," *Nature physics,* vol. 7, no. 2, pp. 138-141, 2011.

[15] Luu, Tran Trung, et al., "Extreme ultraviolet high-harmonic spectroscopy of solids," *Nature,* vol. 521, no. 7553, pp. 498-502, 2015.

[16] Luu, Tran Trung, and Hans Jakob Wörner., "Measurement of the Berry curvature of solids using high-harmonic spectroscopy," *Nature communications,* vol. 9, no. 1, pp. 1-6, 2018.

[17] DeVries, Paul L., "Calculation of harmonic generation during the multiphoton ionization of the hydrogen atom," *JOSA B,* vol. 7, no. 4, pp. 517-520, 1990.

[18] Vampa, G., et al., "Semiclassical analysis of high harmonic generation in bulk crystals," *Physical Review B,* vol. 91, no. 6, p. 064302, 2015.

[19] Golde, Daniel, et al., "Microscopic theory of the extremely nonlinear terahertz response of semiconductors," *physica status solidi (b) ,* vol. 248, no. 4, pp. 863-866, 2011.

[20] Wu, Mengxi, et al., "High-harmonic generation from Bloch electrons in solids," *Physical Review A,* vol. 91, no. 4, p. 043839, 2015.

[21] Franz, Dominik, et al., "All semiconductor enhanced high-harmonic generation from a single nanostructured cone," *Scientific reports,* vol. 9, no. 1, pp. 1-7, 2019.

[22] Liu, Hanzhe, et al., "Enhanced high-harmonic generation from an all-dielectric metasurface," *Nature Physics,* vol. 14, no. 10, pp. 1006-1010, 2018.

[23] Sivis, Murat, et al, "Tailored semiconductors for high-harmonic optoelectronics," *Science* , vol. 357, no. 6348, pp. 303-306, 2017.

[24] Maiman, Theodore H., "Stimulated optical radiation in ruby," *nature,* vol. 187, no. 4736, pp. 493-494, 1960.

[25] Franken, eg PA, et al., "Generation of optical harmonics," *Physical Review Letters ,* vol. 7, no. 4, p. 118, 1961.

[26] He, Xinkui, et al., "Spatial and spectral properties of the high-order harmonic emission in argon for seeding applications," *Physical Review A,* vol. 79, no. 6, p. 063829, 2009.

[27] Mairesse, Y., et al., "Attosecond synchronization of high-harmonic soft x-rays," *Science,* vol. 302, no. 5650, pp. 1540-1543, 2003.

[28] Wikmark, Hampus, et al., "Spatiotemporal coupling of attosecond pulses," *Proceedings of the National Academy of Sciences*, vol. 116, no. 11, pp. 4779-4787, 2019.

[29] Dinh, K. B., and L. V. Dao, *Phase-matched High Order Harmonic Generation and Application*, Nova Publishers Inc. NY., USA, 2013.

[30] Ghimire, Shambhu, and David A. Reis, "High-harmonic generation from solids," *Nature Physics*, vol. 15, no. 1, pp. 10-16, 2019.

[31] Reiss, H. R., "Complete Keldysh theory and its limiting cases," *Physical Review A*, vol. 42, no. 3, p. 1476, 1990.

[32] Vampa, G., et al., "Linking high harmonics from gases and solids," *Nature*, vol. 522, no. 7557, pp. 462-464, 2015.

[33] Kim, Yong Woo, et al., "Spectral interference in high harmonic generation from solids," *ACS Photonics*, vol. 6, no. 4, pp. 851-857, 2019.

[34] Abadie, Christopher Q., Mengxi Wu, and Mette B. Gaarde., "Spatiotemporal filtering of high harmonics in solids," *Optics letters*, vol. 43, no. 21, pp. 5339-5342, 2018.

[35] Hohenleutner, Matthias, et al. , "Real-time observation of interfering crystal electrons in high-harmonic generation," *Nature* , vol. 523, no. 7562, pp. 572-575, 2015.

[36] Garg, Manish, et al., "Multi-petahertz electronic metrology," *Nature*, vol. 538, no. 7625, pp. 359-363, 2016.

[37] You, Yong Sing, et al. , "Laser waveform control of extreme ultraviolet high harmonics from solids," *Optics letters*, vol. 42, no. 9, pp. 1816-1819, 2017.

[38] Saito, Nariyuki, et al., "Observation of selection rules for circularly polarized fields in high-harmonic generation from a crystalline solid," *Optica*, vol. 4, no. 11, pp. 1333-1336, 2017.

[39] Han, Seunghwoi, et al., "Extraction of higher-order nonlinear electronic response in solids using high harmonic generation," *Nature communications*, vol. 10, no. 1, pp. 1-6, 2019.

[40] Vampa, G., et al., "Plasmon-enhanced high-harmonic generation from silicon," *Nature Physics*, vol. 13, no. 7, pp. 659-662, 2017.

[41] Liu, Hanzhe, et al., "High-harmonic generation from an atomically thin semiconductor," *Nature Physics*, vol. 13, no. 3, pp. 262-265, 2017.

[42] Keldysh, L. V. , "Ionization in the field of a strong electromagnetic wave," *Sov. Phys. JETP,* vol. 20, no. 5, pp. 1307-1314, 2965.

[43] Uzan, Ayelet Julie, et al., "Attosecond spectral singularities in solid-state high-harmonic generation," *Nature Photonics,* vol. 14, no. 3, pp. 183-187, 2020.

[44] Vampa, Giulio, et al., "Disentangling interface and bulk contributions to high-harmonic emission from solids," *Optica,* vol. 6, no. 7, pp. 553-556, 2019.

[45] Langer, Fabian, et al., "Symmetry-controlled temporal structure of high-harmonic carrier fields from a bulk crystal," *Nature photonics,* vol. 11, no. 4, p. 227, 2017.

[46] You, Yong Sing, David A. Reis, and Shambhu Ghimire, "Anisotropic high-harmonic generation in bulk crystals," *Nature physics,* vol. 13, no. 4, pp. 345-349, 2017.

[47] Schubert, Olaf, et al., "Sub-cycle control of terahertz high-harmonic generation by dynamical Bloch oscillations," *Nature Photonics,* vol. 8, no. 2, pp. 119-123, 2014.

[48] Garg, Manish, Hee-Yong Kim, and Eleftherios Goulielmakis., "Ultimate waveform reproducibility of extreme-ultraviolet pulses by high-harmonic generation in quartz," *Nature Photonics,* vol. 12, no. 5, pp. 291-296, 2018.

[49] Wu, Mengxi, et al., "Multilevel perspective on high-order harmonic generation in solids," *Physical Review A,* vol. 94, no. 6, p. 063403, 2016.

[50] Sivis, Murat, et al., "Extreme-ultraviolet light generation in plasmonic nanostructures," *Nature Physics,* vol. 9, no. 5, pp. 304-309, 2013.

[51] Han, Seunghwoi, et al., "High-harmonic generation by field enhanced femtosecond pulses in metal-sapphire nanostructure," *Nature communications,* vol. 7, no. 1, pp. 1-7, 2016.

[52] Imasaka, Kotaro, et al., "ntenna-enhanced high harmonic generation in a wide-bandgap semiconductor ZnO," *Optics express,* vol. 26, no. 16, pp. 21364-21374, 2018.

[53] Vampa, G., et al., "Strong-field optoelectronics in solids," *Nature Photonics,* vol. 12, no. 8, pp. 465-468, 2018.

[54] Kim, Hyunwoong, et al., "Generation of coherent extreme-ultraviolet radiation from bulk sapphire crystal," *ACS Photonics* , vol. 4, no. 7, pp. 1627-1632, 2017.

[55] E. Hecht, Optics, San Francisco : Addison Wesley, 2002.

[56] Lalanne, Philippe, and Dominique Lemercier-Lalanne, "On the effective medium theory of subwavelength periodic structures," *Journal of Modern Optics* , vol. 43, no. 10, pp. 2063-2085, 1996.

[57] Lalanne, Philippe, and Dominique Lemercier-Lalanne, "Depth dependence of the effective properties of subwavelength gratings," *JOSA A*, vol. 14, no. 2, pp. 450-459, 1997.

[58] Lalanne, Philippe, and Jean-Paul Hugonin., "High-order effective-medium theory of subwavelength gratings in classical mounting: application to volume holograms," *JOSA A*, vol. 15, no. 7, pp. 1843-1851, 1998.

[59] Kang, Guo Guo, Qiao Feng Tan, and Guo Fan Jin, "Polarization-selective subwavelength grating used with 193 nm light," *Optics communications*, vol. 283, no. 22, pp. 4531-4535, 2010.

[60] Wörner, Hans Jakob, et al., "Following a chemical reaction using high-harmonic interferometry," *Nature*, vol. 466, no. 7306, pp. 604-607, 2010.